Remote Sensing of Environment 229 (2019) 32–47

Contents lists available at ScienceDirect

Remote Sensing of Environment

journal homepage: www.elsevier.com/locate/rse

Chlorophyll algorithms for ocean color sensors - OC4, OC5 & OC6

John E. O'Reilly[a], P. Jeremy Werdell[b,*]

[a] Retired: NOAA National Marine Fisheries Service, Narragansett, RI 02882, USA
[b] NASA Goddard Space Flight Center, Greenbelt, MD 20771, USA

ARTICLE INFO

Keywords:
Satellite remote sensing
Ocean color
Bio-optical algorithms
Ocean optics
Chlorophyll-*a*

ABSTRACT

A high degree of consistency and comparability among chlorophyll algorithms is necessary to meet the goals of merging data from concurrent overlapping ocean color missions for increased coverage of the global ocean and to extend existing time series to encompass data from recently launched missions and those planned for the near future, such as PACE, OLCI, HawkEye, EnMAP and SABIA-MAR. To accomplish these goals, we developed 65 empirical ocean color (OC) chlorophyll algorithms for 25 satellite instruments using the largest available and most globally representative database of coincident *in situ* chlorophyll *a* and remote sensing reflectances. Excellent internal consistency was achieved across these OC 'Version -7' algorithms, as demonstrated by a median regression slope and coefficient of determination (R^2) of 0.985 and 0.859, respectively, among 903 pairwise comparisons of OC-modeled chlorophyll. SeaWiFS and MODIS-Aqua satellite-to-*in situ* match-up results indicated equivalent, and sometimes superior, performance to current heritage chlorophyll algorithms.

During the past forty years of ocean color research the violet band (412 nm) has rarely been used in empirical algorithms to estimate chlorophyll concentrations in oceanic surface water. While the peak in chlorophyll-specific absorption coincides with the 443 nm band present on most ocean color sensors, the magnitude of chlorophyll-specific absorption at 412 nm can reach upwards of ~70% of that at 443 nm. Nearly one third of total chlorophyll-specific absorption between 400 and 700 nm occurs below 443 nm, suggesting that bands below 443 nm, such as the 412 nm band present on most ocean color sensors, may also be useful in detecting chlorophyll under certain conditions and assumptions. The 412 nm band is also the brightest band (that is, with the most dominant magnitude) in remotely sensed reflectances retrieved by heritage passive ocean color instruments when chlorophyll is less than ~0.1 mg m^{-3}, which encompasses ~24% of the global ocean. To attempt to exploit this additional spectral information, we developed two new families of OC algorithms, the OC5 and OC6 algorithms, which include the 412 nm band in the MBR. By using this brightest band in MBR empirical chlorophyll algorithms, the highest possible dynamic range of MBR may be achieved in these oligotrophic areas.

The terms oligotrophic, mesotrophic, and eutrophic get frequent use in the scientific literature to designate trophic status; however, quantitative definitions in terms of chlorophyll levels are arbitrarily defined. We developed a new, reproducible, bio-optically based index for trophic status based on the frequency of the brightest, maximum band in the MBR for the OC6_SEAWIFS algorithm, along with remote sensing reflectances from the entire SeaWiFS mission. This index defines oligotrophic water as chlorophyll less than ~0.1 mg m^{-3}, eutrophic water as chlorophyll *a*bove 1.67 mg m^{-3} and mesotrophic water as chlorophyll between 0.1 and 1.67 mg m^{-3}. Applying these criteria to the 40-year mean global ocean chlorophyll data set revealed that oligotrophic, mesotrophic, and eutrophic water occupy ~24%, 67%, and 9%, respectively, of the area of the global ocean on average.

1. Introduction

Ocean color satellite instruments have provided spatially and temporally comprehensive data on the near-surface distribution of the photosynthetic pigment chlorophyll *a* (CHL; mg m^{-3}) since the launch of the pioneering NASA Coastal Zone Color Scanner (CZCS) on board Nimbus-7 in 1978. This near-continuous, globally-distributed data record plays a key role in continually advancing our scientific understanding of spatial and temporal distributions of phytoplankton and other marine biogeochemical constituents. In particular, ocean color satellite data records have provided novel insights into fundamental aquatic biogeochemical processes (Siegel et al., 2005a; IOCCG, 2009a,

* Corresponding author.
E-mail address: jeremy.werdell@nasa.gov (P.J. Werdell).

https://doi.org/10.1016/j.rse.2019.04.021
Received 1 October 2018; Received in revised form 18 April 2019; Accepted 19 April 2019
Available online 07 May 2019

Acronyms and abbreviations (ocean color sensors are denoted by *)

aCDOM absorption by colored dissolved organic matter (m^{-1})
adg absorption by non-algal particles + colored dissolved organic matter (m^{-1})
aNAP absorption by non-algal particles (m^{-1})
aph absorption by phytoplankton (m^{-1})
bbp backscattering by particles (m^{-1})
CDOM Colored Dissolved Organic Matter
CDR Climate Data Record
CHL concentration of chlorophyll-*a* ($mg\ m^{-3}$)
COCTS* Chinese Ocean Color and Temperature Scanner, (HY-1B)
CW Clear Water
CZCS* Coastal Zone Color Scanner, (NIMBUS-7)
CZI* Coastal Zone Imager
DRL German Aerospace Center
ENMAP* Environmental Mapping and Analysis Program Hyperspectral Imager
GLI* Global Imager (NASDA)
GOCI* Geostationary Ocean Color Imager
Gmean Geometric mean (of log-transformed data)
HawkEye* HawkEye Ocean Color Sensor (SeaHawk Cubesat)
HICO* Hyperspectral Imager for the Coastal Ocean
IDL Interactive Data Language (software)
IOP Inherent Optical Property
IRrs Interpolated Remote Sensing Reflectance (sr^{-1})
MaxB Maximum Band (brightest, dominant band)
MBR Maximum Band Ratio
MERIS* Medium-spectral Resolution, Imaging Spectrometer, (ENVISAT)
MERSI* Medium Resolution Spectral Imager
MISR* Multi Angle Imaging Spectroradiometer
MODIS* Moderate Resolution Imaging Spectroradiometer (Terra and Aqua)
MOS* Modular Optical Scanner (IRS-P3)
NAP Non-algal particles
NetCDF Network Common Data Form [a type of formatted data file]
NLW Normalized Water-Leaving Radiance ($uW\ cm^{-2}\ sr^{-1}\ nm^{-1}$)
NOMAD NASA Bio-Optical Marine Algorithm Data set
OBPG Ocean Biology and Processing Group (NASA-GSFC)
OCI* Ocean Color Imager, (ROCSAT)
OCM* Ocean Colour Monitor, (IRS-P4)
OCTS* Ocean Colour and Thermal Sensor (ADEOS)
OLCI* Ocean and Land Colour Instrument, (Sentinel-3)
OLI* Operational Land Imager
OSMI* Ocean Scanning Multispectral Imager (KOMPSAT-1)
PACE_OCI* PACE Ocean Color Instrument
POLDER* POLarization and Directionality of the Earth Reflectances, (ADEOS)
POLDER_2* Follow-on mission, (ADEOS-2)
RMA Reduced Major Axis ['type-2' linear regression]
Rrs Remote Sensing Reflectance ($\lambda\ sr^{-1}$)
R^2 Correlation coefficient squared (Coefficient of Determination)
SABIA_MAR* Satélites Argentino-Brasileño para Información Ambiental del Mar
SeaWiFS* Sea-viewing Wide Field-of-view Sensor, (SeaStar)
SEABAM SeaWiFS Bio-optical Algorithm Mini-Workshop
SGLI* Second-Generation Global Imager, (GCOM-C-Japan)
SMI Standard Mapped Images [4320 × 2160 pixels]
VIIRS* Visible Infrared Imaging Radiometer Suite (Suomi NPP, JPSS-1)

2009b), enabled estimates of global ocean primary production (Antoine et al., 1996; Behrenfeld et al., 2006; Saba et al., 2011; O'Reilly, 2017), and supported assessments of climate-related changes in phytoplankton dynamics and oceanic production (Behrenfeld et al., 2006, Henson et al., 2009, Uitz et al., 2010, Siegel et al., 2013).

The oceanographic community seeks to refine and develop climate data records (CDRs) of chlorophyll *a* (NRC, 2011) and invests substantially into improving and ensuring the consistency of this derived data product across satellite instruments (IOCCG, 2007). This not only enables development of long-term (multi-decadal) time-series, but also facilitates multi-instrument data merging using overlapping missions (Gregg and Woodward, 1998; Kwiatkowska and Fargion, 2002; IOCCG, 2007; Brewin et al., 2014). Individual ocean color satellite instruments, with their limited duration, cannot usually be used to assess decadal-plus changes (*e.g.*, CZCS: 1978–1986; OCTS: 1996–1997; SeaWiFS: 1997–2010; MERIS: 2002–2012). The merging of data from multiple instruments, however, significantly increases their global coverage, particularly in cloudy areas and seasons, while also enhancing the construction of long time-series. Note that merging CHL data from two, three and four instruments realizes median global coverages of ~15%, ~20%, and ~24%, respectively (Table 1). The value of multi-instrument data products, however, decreases substantially without inter-instrument consistency, which relates to the quality of their calibrations, the consistency and comparability of atmospheric correction methods applied to various sensors, and the consistency of the geophysical data product algorithms applied across instruments.

While ocean color satellite instrument characteristics vary (Table 2), they share common data processing steps and strategies. Briefly, passive satellite ocean color instruments measure the spectral radiance emanating from the top of the atmosphere at discrete visible and infrared wavelengths. In conventional agency standard processing, atmospheric correction algorithms are applied to remove the contribution of the atmosphere from the total signal and produce estimates of remote sensing reflectances (Rrs(λ); sr^{-1}), that is, the light exiting the water normalized to the downwelling irradiance incident on the sea surface (Gordon and Wang, 1994; Mobley et al., 2016). Bio-optical algorithms are then applied to the Rrs(λ) to produce estimates of additional

Table 1
Median daily percent global coverage (Median %) of CHL in 10,239 merged 9 km Standard Mapped Images by various sensors and their combinations (C: CZCS, A: MODIS-Aqua, M: MERIS, O: OCTS, S: SeaWiFS, T: MODIS-Terra, V: VIIRS). All available data from 30 October 1978 to 16 March 2018 were considered.

Sensors	N	Median %
AMST	2711	24.22
AMTV	97	23.73
AMT	703	22.23
ATV	2160	20.93
AST	40	19.34
MST	62	19.17
TV	1	18.18
AV	5	18.16
AMS	6	17.94
AT	3	16.01
ST	763	15.5
AM	3	13.33
T	2	9.36
S	921	7.76
O	223	5.02
C	2539	1.18

Table 2
Ocean color satellite instruments considered in this study. The International Ocean Colour Coordinating Group (IOCCG) provides additional details on each instrument (http://www.ioccg.org).

Instrument	Key wavelengths	Agency/Spacecraft	Mission life
CZCS	443;520;550	NASA/Nimbus-7	1978–1986
OCTS	412;443;490;516;565;667	NASDA/ADEOS	1996–1997
POLDER	443;490;565	CNES/ADEOS	1996–1997
MOS	408;443;485;520;570;615	DLR/IRS-P3	1996–2004
SeaWiFS	412;443;490;510;555;670	NASA-Orbital/Orbview-2	1997–2010
OCI	443;490;510;555	NEC/ROCSAT-1	1999–2004
OSMI	412;443;490;510;555;670	KARI/KOMPSAT-1	1999–2008
OCM; OCM-2[a]	412;443;490;510;555;660	ISRO/IRS-P4; Oceansat-2	1999–2010; 2009–present
MISR	446;557	NASA/Terra	1999–present
MODIS	412;442;488;530;554;666	NASA/Terra; Aqua	1999–present; 2002–present
GLI	412;443;490;520;565;666	NASDA/ADEOS-II	2002–2003
POLDER 2	443;490;565	CNES/ADEOS-II	2002–2003
COCTS	412;443;490;520;565;670	SOA/SZ-3; HY-1B	2002–2004; 2007–present
MERIS	412;442;490;510;560;665	ESA/Envisat	2002–2012
MERSI	412;443;490;520;565;650	CMA-NSMC/FY-3	2008–2015
HICO	416;444;490;513;553;668	ONR-DOD-NASA/ISS	2009–2014
GOCI	412;443;490;555;660;680	KIOST/COMS	2010–present
VIIRS[b]	410;443;486;551	NOAA-NASA/Suomi NPP	2012–present
OLI[c]	443;482;561	USGS-NASA Landsat-8	2013–present
OLCI[d]	413;443;490;510;560;665	ESA-Copernicus/Sentinel-3	2016–present
SGLI	412;443;490;530;565;674	JAXA/GCOM-C	2017–present
HawkEye	412;443;490;510;555;670	NASA-UNCW/SeaHawk	2018-present
EnMAP	424;445;489;490;513;554;672	DLR	2019 launch
SABIA-Mar	412;443;490;510;555;665	CONAE-AEB-INPE	2020 launch
PACE-OCI[e]	412;443;490;510;555;678	NASA	2022 launch

[a] Applicable to OCM-3/Oceansat-3, to be launched in 2018–2019.
[b] Applicable to upcoming versions of VIIRS in the NOAA-NASA JPSS series.
[c] Applicable to OLI onboard Landsat-9, to be launched in 2021.
[d] Applicable to upcoming versions of OLCI in the ESA Sentinel-3 series.
[e] Likely applicable to upcoming hyperspectral instruments, such as the DRL HIS/EnMAP.

geophysical properties, such as spectral marine inherent optical properties (IOPs), namely the absorption and backscattering properties of seawater and its particulate and dissolved constituents (IOCCG, 2006; Werdell et al., 2013, 2018), and chlorophyll *a* (O'Reilly et al., 1998).

Broadly speaking, the community historically employs two algorithmic approaches to derive chlorophyll *a* from Rrs(**λ**), colloquially referred to as empirical algorithms (Dierssen, 2010) and semi-analytical algorithms (SAAs; IOCCG, 2006). Empirical algorithms statistically relate measurements (most often collected *in situ*) of CHL and Rrs(**λ**). A well-known empirical approach follows O'Reilly et al. (1998), where a sequencing blue-to-green ratio of Rrs(**λ**) statistically relates to CHL *via* a polynomial expression. Several additional empirical formulations exist, including (but not limited to) Rrs(**λ**) line-height methods (Hu et al., 2012), linear red-edge ratio methods (Moses et al., 2012, Gitelson et al., 2007, Gilerson et al., 2010, and Dall'Olmo et al., 2005) and artificial neural network methods (Doerffer and Schiller, 2007). Alternatively, semi-analytical algorithms provide estimates of CHL using a combination of empiricism and simplification of the radiative transfer equations (*e.g.*, IOCCG, 2006; Werdell et al., 2018). Most SAAs attempt to estimate simultaneously the magnitudes of CHL (*via* spectral absorption of phytoplankton; aph(**λ**), m^{-1}), spectral backscattering by particles (bbp (**λ**); m^{-1}) and the combined absorption by non-algal particles and colored dissolved organic material (adg(**λ**); m^{-1}). This is typically accomplished by assuming spectral shape functions for all aquatic constituent absorption and scattering components and using linear or nonlinear inversion methods (*e.g.*, the nonlinear least squares optimization method of Levenberg-Marquardt) to retrieve the magnitudes of each constituent required to match the spectral distribution of Rrs(**λ**).

The NASA Ocean Biology Processing Group (OBPG; https://oceancolor.gsfc.nasa.gov) currently employs the approaches of O'Reilly et al. (1998) in combination with Hu et al. (2012) to produce and distribute operationally CHL data products from all ocean color satellites within its scope. The original SeaWiFS CHL algorithm was developed by O'Reilly et al. (1998) and further refined in O'Reilly et al. (2000). Its current version, along with similar band ratio algorithms for OCTS, MERIS, MODIS, and VIIRS, was developed following the release of the NASA bio-Optical Marine Algorithm Dataset (NOMAD; Werdell and Bailey, 2005) and has been used by the OBPG in all of its major reprocessing of data since 2009 (https://oceancolor.gsfc.nasa.gov/reprocessing/). In its 2014 reprocessing, the OBPG augmented their default suite of data products by also producing CHL from Hu et al. (2012), which merges the standard band ratio algorithm with their color index (CI). This refinement is restricted to relatively clear water and currently transitions between the two methods when chlorophyll *a* from CI falls between 0.15 and 0.2 mg m^{-3}. Note this algorithm change applies to all ocean color instruments for which the OBPG is responsible and requires an empirical relationship to shift other satellites' bands to those required as input into CI (*e.g.*, 547 nm for MODIS to 555 nm). The OBPG continues to produce and distribute both CHL products in parallel.

Here, we focus on the algorithm form presented in O'Reilly et al. (1998), with this approach hereinafter referred to as OC. The OC approach can be effectively and consistently applied to all satellite instruments dating back to CZCS (McClain, 2009), as well as all those planned for the future (*e.g.*, PACE Science Definition Team, 2018). The OBPG applies instrument-specific versions of OC to each ocean color satellite within its scope (https://oceancolor.gsfc.nasa.gov/atbd/chlor_a/) and periodically updates the polynomial fit coefficients as new *in situ* data become available. The use of a large, temporally and spatially diverse and common set of *in situ* chlorophyll *a* and Rrs(**λ**) pairs to develop cross-instrument algorithms facilitates the spatial and temporal comparability of overlapping missions. The OBPG last updated the OC coefficients in 2009 using NOMAD. Since that time, the *in situ* data set described in Valente and 42 co-authors (2015) emerged for use in satellite algorithm development, which offers, to our knowledge, the most comprehensive CHL-Rrs(**λ**) data set compiled to date. This data set includes NOMAD, as well as many other data, and thus offers a timely opportunity to derive the next generation of OC algorithm

Table 3
Coefficient of determination (R^2) between modeled and *in situ* CHL for four Rrs band ratios across four CHL ranges. Each band ratio model was empirically fitted to the *in situ* data ((N = 298, 1462, 966, and 2720, respectively, for the four CHL ranges)) using a 4th-order polynomial curve as described in the Methods section. The CHL ranges are indicated in brackets, in units of mg m^{-3}.

Band ratio	[0.012 to 0.1]: R^2	[0.1 to 1.67]: R^2	[1.67 to 77.9]: R^2	[0.012 to 77.9]: R^2
Rrs_{412}:Rrs_{555}	0.480	0.558	0.164	0.734
Rrs_{443}:Rrs_{555}	0.496	0.627	0.276	0.808
Rrs_{490}:Rrs_{555}	0.294	0.648	0.394	0.847
Rrs_{510}:Rrs_{555}	0.040	0.572	0.448	0.823

parameterizations.

The scope of this paper is two-fold. First, we present the derivation of updated and internally consistent versions of the OC suite of algorithms for 25 ocean color satellite sensors, as well as their satellite-to-*in situ* validation results for SeaWiFS and MODIS-Aqua. Second, we present expanded versions of the OC algorithms that make use of additional spectral information when available (wavelengths on or near 412 and 670 nm). Our primary and secondary purposes are to provide modern versions of this core algorithm that better represent spatial and temporal bio-optical diversity than their predecessors and to explore increasing information content through the inclusion of additional wavelengths. We acknowledge that community momentum and focus has diversified beyond chlorophyll *a* (*e.g.*, towards IOPs, marine particle characterization, and carbon stocks), as knowledge of bio-optics, available instrumentation, and computing resources have all improved and new science questions have emerged. We also acknowledge the limitations of an inherent assumption of the OC approach – namely, that all optically relevant seawater constituents, such as non-algal particles (NAP) and colored dissolved organic matter (CDOM), co-vary with chlorophyll *a* – and the general sensitivity of band-ratio algorithms to errors in ocean color atmospheric correction and adjacent bright targets. SAAs have shown substantial promise in their ability to simultaneously retrieve multiple parameters, thus isolating confounding constituent signals that violate the former assumption. And, line-height approaches (specifically, Hu et al., 2012) have shown decreased sensitivity to the latter. Yet, we believe the further refinement of the empirical OC algorithms still makes a substantial and necessary contribution to the field. The OC approach offers a unique opportunity to consistently link global satellite measurements of the marine biosphere from 1978 to present day, an activity that cannot currently be as effectively accomplished using alternative approaches with specialized wavelength requirements. Furthermore, CHL serves as input to many secondary algorithms used to derive other biogeochemical and bio-optical products (*e.g.*, Uitz et al., 2010; Hirata et al., 2011; Werdell et al., 2013) that undoubtedly benefit from well-assured cross-instrument consistency and global representation.

2. Methods

2.1. Maximum band ratio algorithms

It was understood early in the CZCS mission that reliable remotely-sensed estimates of total pigment concentrations (= CHL + phaeopigments) could be obtained over a wide concentration range by using the Rrs_{443}:Rrs_{550} band ratio to estimate concentrations below approximately 1.5 mg m^{-3}, then switching to the Rrs_{520}:Rrs_{550} band ratio above this concentration (Gordon et al., 1983). Note that we indicate wavelength dependency using subscript (that is, Rrs_{443} indicates remote-sensing reflectance at 443 nm). The standard CZCS pigment algorithm switched between two equations that related the two band ratios to total pigment concentrations. The switching, however, generated a discontinuity in pigment estimates at the switching value (Fig. 4 in O'Reilly et al., 1998). To eliminate this artifact when developing algorithms for SeaWiFS, O'Reilly et al. (1998) conceived of maximum band ratio (MBR) algorithms that avoid band switching equations and their discontinuities by relating reflectance band ratios to CHL using a single fourth-order polynomial equation that encompasses a wide range of global CHL. Its form follows:

$$\log_{10}(CHL) = a_0 + a_1X + a_2X^2 + a_3X^3 + a_4X^4, \quad (1)$$

where $a_{0..4}$ are the polynomial fit coefficients and X is:

$$X = \log_{10}\left(\frac{R_{rs}(\lambda_b)}{R_{rs}(\lambda_g)}\right). \quad (2)$$

In Eq. (2), $\boldsymbol{\lambda}_b$ and $\boldsymbol{\lambda}_g$ refer to a violet-blue and green wavelength, respectively (with b and g adopted as subscripts based on heritage use of strictly blue and green wavelengths). The blue wavelength is most often the maximum Rrs value over a defined range and the green wavelength is usually the instrument band that falls within 545 and 570 nm. Using SeaWiFS as an example, the maximum band ratio version of Eq. (2) becomes:

$$X = \log_{10}\left(\frac{\max[Rrs_{443}, Rrs_{490}, Rrs_{510}]}{Rrs_{555}}\right) \quad (3)$$

This SeaWiFS OC algorithm was referred to as OC4, where the "4" indicates that four Rrs($\boldsymbol{\lambda}$) are considered in Eq. (3). Currently, the full suite of OC algorithms employs from two to four wavelengths. The three-band version, OC3, uses the MBR of bands near 443 and 490 nm, while the two-band version, OC2, the CHL algorithm initially adopted by NASA for SeaWiFS, assigns $\boldsymbol{\lambda}_b$ as the wavelength nearest to 490 nm.

As a simple illustration of how the $\boldsymbol{\lambda}_b$ to $\boldsymbol{\lambda}_g$ ratio varies and why 490 nm is assigned as $\boldsymbol{\lambda}_b$ in OC2, Table 3 presents the relationships between *in situ* CHL and several two-band models that use the ratio of the violet (412 nm), blue (443 nm), cyan (490 nm), and cyan/green (510 nm) regions of the ocean color spectrum to the green region (555 nm). Note that the dataset is described in detail below. Of these four band ratios, the Rrs_{490}:Rrs_{555} band ratio model yielded the highest coefficient of determination (R^2) with *in situ* CHL when considering the full range of measured CHL in our dataset (Table 3). Relatively lower R^2 were obtained for the remaining three CHL ranges for all the band ratios, as a consequence of the small sample sizes of these subsets. When considering the lowest CHL range (0.012 to 0.1 mg m^{-3}, representative of the most oligotrophic conditions) the highest R^2 was found for the Rrs_{412}:Rrs_{555} and Rrs_{443}:Rrs_{555} band ratios, with the latter only slightly higher than the former. The Rrs_{490}:Rrs_{555} band ratio had the highest R^2 for $0.1 < CHL < 1.67$ mg m^{-3} (mesotrophic), whereas the Rrs_{510}:Rrs_{555} ratio had the highest R^2 for CHL exceeding 1.67 mg m^{-3} (eutrophic) (Table 3).

2.2. In situ data source

We acquired the 'satbands_6_nm.tab' database file from the Valente and 42 co-authors (2015) datasets, which provides observations with spectral information aggregated to within 6 nm of the instrument band centers of SeaWiFS, MODIS, and MERIS. We specifically focused on the SeaWiFS subset of the Valente database, which consists of 2720 paired CHL and Rrs($\boldsymbol{\lambda}$) observations. When available, we preferentially selected high performance liquid chromatography (HPLC) measurements of CHL over fluorometric measurements. The final dataset we used to develop Version -7 of the OC algorithms included 1341 HPLC and 1379 fluorometric observations of CHL that range from 0.012 to 77.9 mg m^{-3}. The assigned version number historically refers to the database used to tune statistically the polynomial coefficients of the OC algorithms (Eq. (1)). The Version -1 algorithms were tuned to the SEABAM dataset which had 919 *in situ* measurements of CHL and Rrs ($\boldsymbol{\lambda}$) (O'Reilly et al., 1998). The Version -4 dataset had 2853 paired observations from an extended version of SEABAM (O'Reilly et al.,

2000) and the Version -6 dataset had 1948 *in situ* observations from NOMAD (Werdell and Bailey, 2005). For reference, the OC versions adopted by NASA in 2009 for their standard processing are Version -6.

2.3. Chlorophyll a (CHL)

The relative frequency distribution of the 2720 *in situ* CHL data used for algorithm tuning is illustrated in Fig. 1, along with the relative frequency distribution of CHL from satellite data collected by seven ocean color sensors during the past forty years. We acquired global, daily satellite standard mapped images (SMI, 9-km spatial resolution) from the NASA OBPG. Both distributions span nearly four orders-of-magnitude; however the *in situ* data have a broader distribution and a higher geometric mean (Gmean) and median (Gmean = 0.861 mg m^{-3}, median = 0.890 mg m^{-3}) than the satellite data (Gmean = 0.1796 mg m^{-3}, median = 0.1740 mg m^{-3}) and have relatively more CHL values above 1 mg m^{-3} than the remotely-sensed data.

2.4. Remote sensing reflectances

The SeaWiFS subset of Valente and 42 co-authors (2015) provides Rrs(λ) at 412, 443, 490, 510, 555 and 670 nm. For reference, Fig. 2 illustrates the arithmetic mean, geometric mean, and median Rrs for this dataset. These spectra illustrate that the geometric mean of Rrs better represents the median than the arithmetic mean, suggesting that the Rrs data for all six SeaWiFS bands are log-normally distributed and that geometric means better indicate the central tendency of their distributions than arithmetic means. Generation of OC Version -7 coefficients for all of the satellite instruments of interest requires Rrs elsewhere in the spectrum than what exists in this dataset. While it remains undesirable to estimate Rrs at wavelengths not directly measured, doing so remains unavoidable within an activity such as this that relies on large and diverse data sets (diverse in time, instrument manufacturer, and data collector) and maintains a requirement to capture and consistently address as many spectrally diverse ocean color satellite instruments as possible. Using this dataset and the INTERPOL routine in IDL Version 8.7, we generated 273 interpolated data values (IRrs), between 408 and 680 nm to match the band centers of all satellite instruments of interest (Table 2), as elaborated upon below. We acknowledge that alternate methods exist to estimate Rrs, such as the band-shift approach of Melin and Sclep (2015), but such methods require bio-optical models that cannot be unequivocally applied across all water types in a dataset at diverse at Valente and 42 co-authors (2015) without careful evaluation (and no certain promise of reduced uncertainties or improvement in a ratio-ing algorithm). Consideration of these alternate methods should be included in a subsequent study.

The interpolation method used to generate IRrs data from Rrs data is a prime determinant of the accuracy and comparability of our CHL algorithms. We investigated two methods for interpolating IRrs estimates from the measured Rrs data in our dataset: a linear interpolation of the untransformed Rrs data to yield IRrs (hereafter referred to as the 'Linear' method), and a linear interpolation of log-transformed Rrs data followed by anti-logging the interpolated values to derive IRrs (hereafter referred to as the 'LOG' method). Table 4 presents statistical regression results of a test to explore and evaluate these two methods. The test is based on a two-point interpolation scheme to estimate IRrs from adjacent measured Rrs values from the SeaWiFS subset for the 443, 490, 510, and 555 nm bands, followed by a statistical comparison of the IRrs value with the measured Rrs value for the SeaWiFS band within the interpolation interval. These comparisons provide useful information for comparing the relative performance of these two interpolation methods. Note that the distances between measured Rrs values in this 2-point test (78, 67, 65, and 160 nm) are much greater than the distances between measured Rrs actually used in our final interpolation (31, 47, 20, 45, and 115 nm) across the six SeaWiFS bands. Table 4 shows that the Linear interpolation method results in high R^2 and regression slopes near 1.0 when the interpolation distance is between 65 and 78 nm, but relatively low R^2 and slopes that deviate from 1.0 when interpolating the IRrs for the 555 nm band across the relatively large interval from 510 nm to 670 nm (a 160 nm span). The LOG method results in higher R^2 and slopes closer to unity than the Linear method for this wide 510–670 nm interpolation interval, as well as comparable performance metrics elsewhere in the spectrum (Table 4).

Based on the exploratory results presented in Table 4 and the log-normal nature of the Rrs data shown in Fig. 2, we adopted the LOG interpolation method to generate the 273 IRrs data used to tune the CHL algorithms. IRrs values were calculated for each of the 2720 records in the SeaWiFS *in situ* subset where all six Rrs measurements were greater than zero. It is important to stress that the IRrs values are identical to the measured Rrs values at the six SeaWiFS bands since the interpolation passes through each of these measured Rrs data points. To evaluate the accuracy of our interpolated IRrs values, we compared our derived IRrs values with measured Rrs data available in the SeaWiFS, MERIS, and MODIS subsets of the Valente and 42 co-authors (2015) database (Table 5). A slope value of 1.0 indicates that the IRrs data for that sensor are identical to the SeaWiFS Rrs data. The remaining nine slopes range between 0.9195 and 1.0053, indicating an approximate accuracy for the IRrs values of between 1 and 8%. The exact error contributed by the use of interpolated data (IRrs) in the 65 CHL algorithms we developed, however, remains difficult to quantify, as 61 of these used one or more IRrs values that were identical to the un-interpolated SeaWiFS Rrs in the original Valente data set (Table 5).

2.5. Algorithm tuning

Our tuning of the OC algorithms used 2720 pairs of coincident CHL and IRrs. We tuned the fourth-order polynomial regression coefficients (Eq. (1)) for each algorithm model by using an IDL minimization routine (AMOEBA) to achieve simultaneously: a slope of 1; an intercept of 0; a maximum R^2 for the Reduced Major Axis linear regression between the log-transformed measured CHL and log-transformed model CHL; and, a minimum root mean square error between log-transformed measured CHL and log-transformed model CHL quantiles. The final

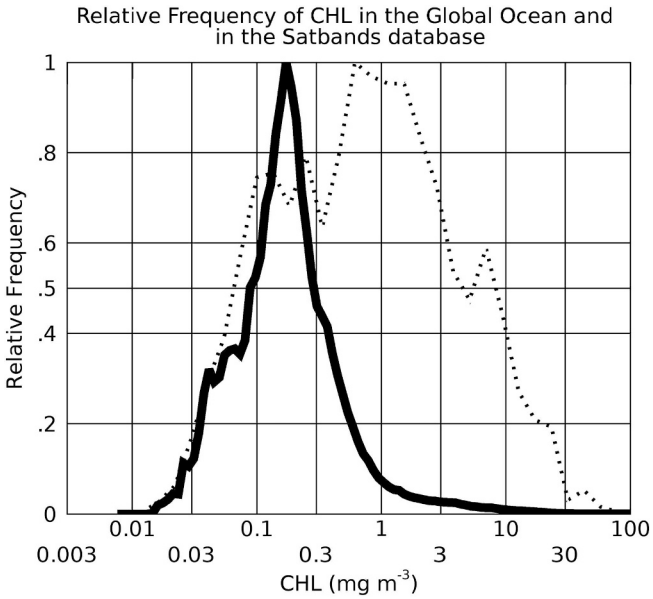

Fig. 1. Relative frequency distributions of CHL for the *in situ* database used to tune the algorithms (dotted curve) and for the forty-year geometric mean of SMI pixels from CHL data for the period from 1978-10-30 to 2018-03-16, based on 24,455 NASA Level-3 global daily SMI netCDF images from seven satellite instruments: CZCS, OCTS, SeaWiFS, MODIS-Terra, MODIS-Aqua, MERIS & VIIRS (solid black curve).

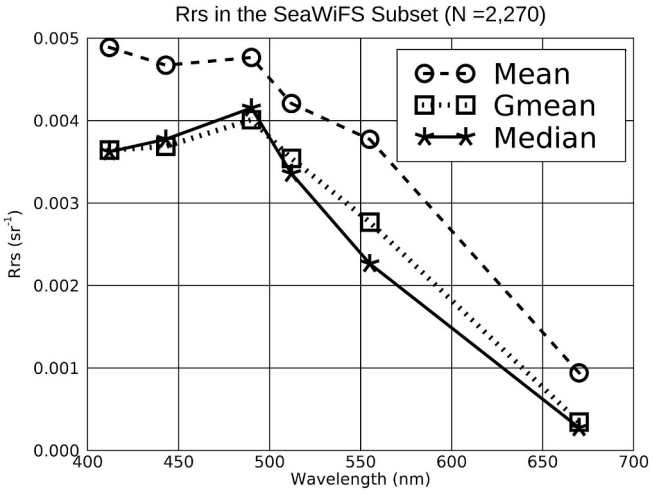

Fig. 2. A comparison of the mean, geometric mean (Gmean), and median of the 2720 Rrs values for the six bands in the SeaWiFS subset of the Valente and 42 co-authors (2015) dataset.

polynomial fit approximates a Type-2 non-linear regression that assumes errors in both the x (MBR) and y (CHL) variables. Excellent reproducibility of results was achieved by specifying double precision computation during curve fitting. One hundred replicate runs for OC4_SEAWIFS yielded five polynomial coefficients as well as linear regression slopes, intercepts, and R^2 between log-transformed measured CHL and log-transformed model CHL that were identical to the fifth decimal place. All 100 replicate runs required the same number of iterations (688) to reach a stable minimization-solution.

2.6. Clear water anchor points

Seven additional clear water data points were added to the 2720 CHL-IRrs pairs during tuning to extrapolate and anchor the curve below the lowest measured CHL (0.012 mg m^{-3}) such that the algorithm ranges encompass the most oligotrophic oceanic waters (Claustre and Maritorena, 2003). We adopted 0.0001 mg m^{-3} for the clear water CHL value, approximately two-orders-of magnitude below the lowest measured CHL in our dataset. This value for the clear water CHL was operationally defined to be the CHL that yielded smooth, extrapolated model curves with monotonically decreasing modeled CHL with increasing MBR. For the corresponding clear water MBR value, we computed clear water reflectances at λ_b and λ_g for each algorithm following Morel and Maritorena (2001). For example, the clear water reflectance ratio for OC4_SEAWIFS (21.35) used Rrs_{443} and Rrs_{555} and the clear water reflectance ratio for OC5_SEAWIFS (33.98) used Rrs_{412} and Rrs_{555}. We acquired seawater absorption values from 350 to 550 nm from Lee et al. (2015) (their Table 1) and above 550 nm from Pope and Fry (1997). We tabulated seawater backscattering measurements using publicly available software (http://finalfrontier.ucsd.edu/Projects/NF-POGO/morel2001.pro, courtesy of Stephane Maritorena) that is based on Morel (1974). The seven clear water data points were excluded from the combined set after tuning so they did not affect final statistical results.

Table 5
Reduced Major Axis linear regression comparisons between interpolated IRrs estimates (LOG method) and measured Rrs data available in the MERIS or MODIS subsets of the Valente and 42 co-authors (2015) database (The regression used log-transformed data).

PAIR	N	INT	SLOPE	R^2
Rrs_{412}_MERIS *versus* $IRrs_{412}$	2720	0	1	1
Rrs_{442}_MERIS *versus* $IRrs_{442}$	2720	0	1.0025	0.9999
Rrs_{490}_MERIS *versus* $IRrs_{490}$	2720	0	1	1
Rrs_{510}_MERIS *versus* $IRrs_{510}$	2720	0	1	1
Rrs_{560}_MERIS *versus* $IRrs_{560}$	2720	0	0.9346	0.9986
Rrs_{620}_MERIS *versus* $IRrs_{620}$	1392	0.0003	0.9551	0.9774
Rrs_{665}_MERIS *versus* $IRrs_{665}$	2720	0	1.0053	0.9983
Rrs_{412}_MODIS *versus* $IRrs_{412}$	2720	0	1	1
Rrs_{443}_MODIS *versus* $IRrs_{443}$	2720	0	1	1
Rrs_{488}_MODIS *versus* $IRrs_{488}$	2720	0	0.9913	0.9995
Rrs_{531}_MODIS *versus* $IRrs_{531}$	1248	0.0001	0.9559	0.9979
Rrs_{547}_MODIS *versus* $IRrs_{547}$	798	0.0001	0.9652	0.9985
Rrs_{667}_MODIS *versus* $IRrs_{667}$	2720	0	0.994	0.9986
Rrs_{678}_MODIS *versus* $IRrs_{678}$	1619	−0.0001	0.9195	0.9731
Rrs_{412}_SEAWIFS *versus* $IRrs_{412}$	2720	0	1	1
Rrs_{443}_SEAWIFS *versus* $IRrs_{443}$	2720	0	1	1
Rrs_{490}_SEAWIFS *versus* $IRrs_{490}$	2720	0	1	1
Rrs_{510}_SEAWIFS *versus* $IRrs_{510}$	2720	0	1	1
Rrs_{555}_SEAWIFS *versus* $IRrs_{555}$	2720	0	1	1
Rrs_{670}_SEAWIFS *versus* $IRrs_{670}$	2720	0	1	1

2.7. Long-term CHL means

Passive ocean color satellite instruments rely on daylight for measurements of remote-sensing reflectances. Consequently, there are significant regional, seasonal, and latitudinal differences and biases in chlorophyll retrievals from these instruments (Gregg and Casey, 2007). Seasonal or inter-annual variations in cloud cover, for example, can influence long-term averages in various geographic regions. Diurnal variability can contribute to differences in retrievals from, for example, SeaWiFS (13:00 local overpass time) compared to MERIS (10:00 local overpass time) as well. The following statistical averaging strategy was employed to minimize latitudinal and seasonal biases and gaps in coverage when computing long-term means:

1) Daily, global SMI data (4502 days) were first averaged by pixel by month. For the SeaWiFS mission there were 157 available months. For the 40-year CHL mean there were 347 available months;
2) The monthly means were then averaged by pixel, by month, to form 12 climatological monthly means; and,
3) The 12 climatological monthly means were then averaged by pixel to compute the long-term means.

Table 4
Reduced Major Axis linear regression comparisons between log-transformed IRrs estimates from two adjacent Rrs values and measured Rrs data available in the SeaWiFS subset of the Valente and 42 co-authors (2015) database.

Lower Rrs	Upper Rrs	Distance (nm)	Interpolated IRrs	Method	N	INT	SLOPE	R^2
412	490	78	443	Linear	2720	−0.0831	0.9565	0.9879
443	510	67	490	Linear	2720	−0.1561	0.9486	0.9739
490	555	65	510	Linear	2720	0.0405	1.007	0.9561
510	670	160	555	Linear	2720	−0.5623	0.7805	0.7159
412	490	78	443	LOG	2720	−0.0718	0.9659	0.9853
443	510	67	490	LOG	2720	−0.1929	0.9384	0.967
490	555	65	510	LOG	2720	0.0036	1.0017	0.9844
510	670	160	555	LOG	2720	−0.3581	0.9283	0.9375

CHL data were log-transformed during averaging as this provided the best estimator of the central tendency of the frequency distribution of the data (that is, the geometric mean was similar to the median of the distribution).

3. Results

We derived 65 OC algorithms encompassing 25 satellite ocean color sensors: COCTS, CZCS, ENMAP, GLI, GOCI, HAWKEYE, HICO, MERIS, MERSI, MISR, MODIS, MOS, OCI, OCM, OCTS, OLCI, OLI, OSMI,

Table 6
Sixty-five OC maximum band ratio and band ratio algorithms. M, R^2, and A represent the mean of Rrs from two bands in the denominator of the OC6 formulas, the coefficient of determination between log-transformed measured and modeled CHL, and the polynomial coefficients for Eq. (1), respectively (in the formulas for OC6 algorithms, M(555&670), for example, represents the mean of Rrs_{555} and Rrs_{670}).

Algorithm	Formula	R^2	A
OC6_SEAWIFS	MBR = Rrs(412 > 443 > 490 > 510)/M(555&670)	0.8508	0.92160; −3.17884; 2.39690; −1.30318; 0.20160
OC6_MODIS	MBR = Rrs(412 > 442 > 488 > 531)/M(554&667)	0.8463	1.22914; −4.99423; 5.64706; −3.53426; 0.69266
OC6_MERIS	MBR = Rrs(412 > 442 > 490 > 510)/M(560&665)	0.8519	0.95087; −3.05489; 2.18141; −1.11783; 0.15132
OC6_COCTS	MBR = Rrs(412 > 443 > 490 > 520)/M(565&670)	0.8504	1.11801; −3.48138; 2.74672; −1.38603; 0.19322
OC6_SGLI	MBR = Rrs(412 > 443 > 490 > 530)/M(565&674)	0.847	1.28506; −4.20996; 3.83254; −2.03507; 0.32442
OC6_SABIA_MAR	MBR = Rrs(412 > 443 > 490 > 510)/M(555&665)	0.8512	0.90755; −3.17549; 2.43524; −1.34385; 0.21096
OC6_PACE_OCI	MBR = Rrs(412 > 443 > 490 > 510)/M(555&678)	0.8502	0.94297; −3.18493; 2.33682; −1.23923; 0.18697
OC6_OSMI	MBR = Rrs(412 > 443 > 490 > 510)/M(555&670)	0.8508	0.92160; −3.17884; 2.39690; −1.30318; 0.20160
OC6_OLCI	MBR = Rrs(413 > 443 > 490 > 510)/M(560&665)	0.8525	0.95039; −3.05404; 2.17992; −1.12097; 0.15262
OC6_OCTS	MBR = Rrs(412 > 443 > 490 > 516)/M(565&667)	0.8514	1.05968; −3.24992; 2.41784; −1.19442; 0.15412
OC6_OCM	MBR = Rrs(412 > 443 > 490 > 510)/M(555&660)	0.8515	0.89280; −3.17118; 2.47461; −1.38801; 0.22203
OC6_MOS	MBR = Rrs(408 > 443 > 485 > 520)/M(570&615)	0.8493	0.95411; −3.45810; 2.95256; −1.35470; 0.07931
OC6_MERSI	MBR = Rrs(412 > 443 > 490 > 520)/M(565&650)	0.8519	1.05578; −3.52403; 3.02209; −1.63058; 0.24777
OC6_HICO	MBR = Rrs(416 > 444 > 490 > 513)/M(553&668)	0.8529	0.96178; −3.43787; 2.80047; −1.59267; 0.26869
OC6_HAWKEYE	MBR = Rrs(412 > 443 > 490 > 510)/M(555&670)	0.8508	0.92160; −3.17884; 2.39690; −1.30318; 0.20160
OC6_GOCI	MBR = Rrs(412 > 443 > 490 > 555)/M(660&680)	0.7906	1.60887; −1.68050; −0.31117; 0.56459; −0.15294
OC6_GLI	MBR = Rrs(412 > 443 > 490 > 520)/M(565&666)	0.8508	1.10656; −3.48994; 2.79927; −1.43087; 0.20257
OC6_ENMAP	MBR = Rrs(424 > 445 > 489 > 513)/M(554&672)	0.8563	0.96229; −3.38589; 2.66366; −1.50367; 0.24946
OC5_SEAWIFS	MBR = Rrs(412 > 443 > 490 > 510)/Rrs555	0.8364	0.33899; −3.11338; 3.35701; −2.01792; −0.03811
OC5_OLCI	MBR = Rrs(413 > 443 > 490 > 510)/ Rrs 560	0.8437	0.43213; −3.13001; 3.05479; −1.45176; −0.24947
OC5_MODIS	MBR = Rrs(412 > 442 > 488 > 531)/ Rrs 554	0.8307	0.42919; −4.88411; 9.57678; −9.24289; 2.51916
OC5_MERIS	MBR = Rrs(412 > 442 > 490 > 510)/ Rrs 560	0.8429	0.43282; −3.12934; 3.04872; −1.43479; −0.25474
OC5_GOCI	MBR = Rrs(412 > 443 > 490 > 555)/ Rrs 660	0.793	1.60197; −1.80486; −0.37900; 0.72207; −0.20484
OC5_SABIA_MAR	MBR = Rrs(412 > 443 > 490 > 510)/ Rrs 555	0.8364	0.33899; −3.11338; 3.35701; −2.01792; −0.03811
OC5_PACE_OCI	MBR = Rrs(412 > 443 > 490 > 510)/ Rrs 555	0.8364	0.33899; −3.11338; 3.35701; −2.01792; −0.03811
OC5_OSMI	MBR = Rrs(412 > 443 > 490 > 510)/ Rrs 555	0.8364	0.33899; −3.11338; 3.35701; −2.01792; −0.03811
OC5_GLI	MBR = Rrs(412 > 443 > 490 > 520)/ Rrs 565	0.8479	0.57617; −3.72075; 4.39869; −2.57369; 0.10102
OC5_ENMAP	MBR = Rrs(424 > 445 > 489 > 513)/ Rrs 554	0.8436	0.33638; −3.34851; 4.17646; −3.10417; 0.32935
OC5_COCTS	MBR = Rrs(412 > 443 > 490 > 520)/ Rrs 565	0.8479	0.57617; −3.72075; 4.39869; −2.57369; 0.10102
OC5_HAWKEYE	MBR = Rrs(412 > 443 > 490 > 510)/ Rrs 555	0.8364	0.33899; −3.11338; 3.35701; −2.01792; −0.03811
OC5_HICO	MBR = Rrs(416 > 444 > 490 > 513)/ Rrs 553	0.8389	0.34355; −3.40385; 4.34820; −3.26853; 0.41553
OC5_MERSI	MBR = Rrs(412 > 443 > 490 > 520)/ Rrs 565	0.8479	0.57617; −3.72075; 4.39869; −2.57369; 0.10102
OC5_MOS	MBR = Rrs(408 > 443 > 485 > 520)/ Rrs 570	0.8465	0.66874; −3.67737; 3.84550; −1.77616; −0.13769
OC5_OCM	MBR = Rrs(412 > 443 > 490 > 510)/ Rrs 555	0.8364	0.33899; −3.11338; 3.35701; −2.01792; −0.03811
OC5_OCTS	MBR = Rrs(412 > 443 > 490 > 516)/ Rrs 565	0.8477	0.55123; −3.44308; 3.61405; −1.78572; −0.15201
OC4_SEAWIFS	MBR = Rrs(443 > 490 > 510)/Rrs555	0.8508	0.32814; −3.20725; 3.22969; −1.36769; −0.81739
OC4_COCTS	MBR = Rrs(443 > 490 > 520)/Rrs565	0.8603	0.57049; −3.79984; 4.25538; −1.87362; −0.62622
OC4_VIIRS	MBR = Rrs(410 > 443 > 486)/Rrs551	0.8245	0.26101; −2.53974; 1.63454; −0.21157; −0.66549
OC4_SGLI	MBR = Rrs(412 > 443 > 490)/Rrs565	0.8411	0.43171; −2.46496; 1.25461; 0.36690; −0.80127
OC4_SABIA_MAR	MBR = Rrs(443 > 490 > 510)/Rrs555	0.8508	0.32814; −3.20725; 3.22969; −1.36769; −0.81739
OC4_OCM	MBR = Rrs(443 > 490 > 510)/Rrs555	0.8508	0.32814; −3.20725; 3.22969; −1.36769; −0.81739
OC4_OCI	MBR = Rrs(443 > 490 > 510)/Rrs555	0.8508	0.32814; −3.20725; 3.22969; −1.36769; −0.81739
OC4_MOS	MBR = Rrs(443 > 485 > 520)/Rrs570	0.861	0.66316; −3.75896; 3.67693; −1.03117; −0.84256
OC4_MERSI	MBR = Rrs(443 > 490 > 520)/Rrs565	0.8603	0.57049; −3.79984; 4.25538; −1.87362; −0.62622
OC4_HICO	MBR = Rrs(444 > 490 > 513)/Rrs553	0.8506	0.33527; −3.48692; 4.20858; −2.64340; −0.35546
OC4_HAWKEYE	MBR = Rrs(443 > 490 > 510)/Rrs555	0.8508	0.32814; −3.20725; 3.22969; −1.36769; −0.81739
OC4_GOCI	MBR = Rrs(412 > 443 > 490)/Rrs555	0.8313	0.28043; −2.49033; 1.53980; −0.09926; −0.68403
OC4_GLI	MBR = Rrs(443 > 490 > 520)/Rrs565	0.8603	0.57049; −3.79984; 4.25538; −1.87362; −0.62622
OC4_ENMAP	MBR = Rrs(445 > 490 > 513)/Rrs554	0.8506	0.33518; −3.42262; 3.96328; −2.20298; −0.61986
OC4_PACE_OCI	MBR = Rrs(443 > 490 > 510)/Rrs555	0.8508	0.32814; −3.20725; 3.22969; −1.36769; −0.81739
OC4_MERIS	MBR = Rrs(442 > 490 > 510)/Rrs560	0.8564	0.42487; −3.20974; 2.89721; −0.75258; −0.98259
OC4_OLCI	MBR = Rrs(443 > 490 > 510)/Rrs560	0.8566	0.42540; −3.21679; 2.86907; −0.62628; −1.09333
OC4_OCTS	MBR = Rrs(443 > 490 > 516)/Rrs565	0.8601	0.54655; −3.51799; 3.39128; −0.91567; −0.97112
OC4_OSMI	MBR = Rrs(443 > 490 > 510)/Rrs555	0.8508	0.32814; −3.20725; 3.22969; −1.36769; −0.81739
OC4_MODIS	MBR = Rrs(412 > 442 > 488)/Rrs554	0.8292	0.27015; −2.47936; 1.53752; −0.13967; −0.66166
OC3_POLDER	MBR = Rrs(443 > 490)/Rrs565	0.8546	0.41712; −2.56402; 1.22219; 1.02751; −1.56804
OC3_VIIRS	MBR = Rrs(443 > 486)/Rrs551	0.843	0.23548; −2.63001; 1.65498; 0.16117; −1.37247
OC3_CZCS	MBR = Rrs(443 > 520)/Rrs550	0.8436	0.31841; −4.56386; 8.63979; −8.41411; 1.91532
OC3_SGLI	MBR = Rrs(443 > 490)/Rrs565	0.8546	0.41712; −2.56402; 1.22219; 1.02751; −1.56804
OC3_POLDER_2	MBR = Rrs(443 > 490)/Rrs565	0.8546	0.41712; −2.56402; 1.22219; 1.02751; −1.56804
OC3_MODIS	MBR = Rrs(442 > 488)/Rrs554	0.8454	0.26294; −2.64669; 1.28364; 1.08209; −1.76828
OC3_OLI	MBR = Rrs(443 > 482)/Rrs561	0.8466	0.30963; −2.40052; 1.28932; 0.52802; −1.33825
OC2_POLDER	BR = Rrs(443/Rrs565)	0.8174	0.19868; −1.78301; 0.84573; 0.19455; −0.95628
OC2_POLDER_2	BR = Rrs(443/Rrs565)	0.8174	0.19868; −1.78301; 0.84573; 0.19455; −0.95628
OC2_MISR	BR = Rrs(446/Rrs557)	0.8126	0.10922; −1.82977; 0.95797; 0.00543; −1.13850

PACE_OCI, POLDER, POLDER_2, SABIA_MAR, SEAWIFS, SGLI, and VIIRS (see Acronyms and Abbreviations and Table 2). Several algorithms were generated for each instrument, defined by the number of wavelengths employed (*e.g.*, versions of OC6, OC5 and, OC4 for SeaWiFS). For brevity, we limit much of our presentation of results to SeaWiFS OC4, OC5, and OC6. Given our use of a constant (invariant) approach to tune each OC algorithm and given that many of the results presented in Table 6 simply update previous fit coefficients, we believe a discussion of results for SeaWiFS alone represents many of the results for the updated OC algorithms. Both OC5 and OC6 merit specific attention as they employ more spectral information than previous OC algorithms. We also explore algorithm consistencies and present validation results for several sensors.

3.1. OC4_SEAWIFS

Version -7 of the OC4_SEAWIFS MBR algorithm is illustrated in Fig. 3. The R^2 between measured and model-CHL is 0.851. This is lower than that for Version -1 (0.932), and Version -4 (0.892), most likely because Version -7 encompasses greater bio-optical diversity than is present in the earlier datasets. The OC4_SEAWIFS MBR algorithm provides a useful illustration of how maximum band ratio algorithms operate (Fig. 3b and Fig. 4): at low CHL, the 443 nm band dominates over the 490 nm and 510 nm bands; whereas at intermediate CHL, between ~0.3 and ~1.5 mg m^{-3}, the 490 nm band dominates; and, at high CHL concentrations, above approximately 1.6 mg m^{-3}, the 510 nm dominates. By using the brightest band – that is, the greatest of Rrs_{443}, Rrs_{490} or Rrs_{510} in the numerator of the MBR (Eq. (3)) – OC4 maintains the highest possible dynamic range (in a way, offering the highest possible signal-to-noise) over nearly four orders-of-magnitude range in chlorophyll concentration. Maximum band ratio algorithms such as OC4 are effective over a wide range in CHL because accessory pigments such as carotenoids, which absorb at longer wavelengths than CHL, are correlated with CHL (Aiken et al., 1995).

3.2. OC5_SEAWIFS

Rrs_{412} has infrequently been used in empirical CHL algorithms. We are aware of one study that evaluated its use (Siswanto et al., 2011). Our OC5 algorithms, such as OC5_SEAWIFS (Fig. 5), exploit up to four bands in the numerator of the MBR and one band in the denominator. In addition to the blue (443 nm), cyan (490 nm) and cyan/green (510 nm) bands used in OC4, OC5 uses the violet (412 nm) band. Rrs_{412} is generally greater than Rrs_{443} and, therefore, dominates the MBR from lowest CHL to approximately 0.3 mg m^{-3}. Consequently, the role played by Rrs_{443} in OC5 is subordinate to that played by Rrs_{412}. Similar to OC4, Rrs_{490} dominates over other bands at intermediate levels of CHL from ~0.3 to ~1.6 mg m^{-3} and Rrs_{510} generally dominates above ~1.6 mg m^{-3}. The R^2 for OC5 (0.838) is slightly less than that for OC4 (0.851); however, the magnitude of the MBR for OC5 is greater than that for OC4, suggesting that the signal-to-noise at low CHL (offered by this increase in dynamic range) is likely better for OC5 than OC4.

3.3. OC6_SEAWIFS

OC6 algorithms, such as OC6_SEAWIFS (Fig. 6), use the same bands in the numerator of its MBR as OC5_SEAWIFS. OC6_SEAWIFS, however, employs the mean of Rrs_{555} and Rrs_{670} in the denominator of the MBR, approximating radiances for a band at 613 nm. Consequently, the MBR ratios are greater with this shift to bands with longer wavelengths and lower Rrs. The R^2 between model and *in situ* data for OC6_SEAWIFS (0.851) is slightly higher than the R^2 for OC5_SEAWIFS (0.836) and equivalent to that of OC4_SEAWIFS. The variation in the dominant band with variation in CHL is illustrated for OC6_SEAWIFS in Fig. 6b and Fig. 7. Because OC5_SEAWIFS has the same bands in the numerator of its MBR as OC6_SEAWIFS, its dominant bands are similar to OC6_SEAWIFS. The high degree of overlap in the dominant band in the OC4, OC5 and OC6 algorithms minimizes the potential for artifacts, such as discontinuities from shifts in the brightest band used in the MBR. For comparison, the global distributions of CHL from OC6_SEAWIFS and OC4_SEAWIFS, based on Rrs data from the entire SeaWiFS mission, are provided in Fig. 8.

3.4. Maximum band ratio algorithms

In addition to the CHL algorithms for SeaWiFS reviewed above, instrument-specific OC algorithms were developed for 24 other ocean color sensors. Table 6 summarizes the bands (wavelengths) used, the formulas, the R^2, and the polynomial coefficients derived for 65 Version -7 OC algorithms. The R^2 between the log-transformed *in situ* CHL and the log-transformed model CHL ranged between 0.791 and 0.861. Forty-three of these employ unique combinations of bands in their

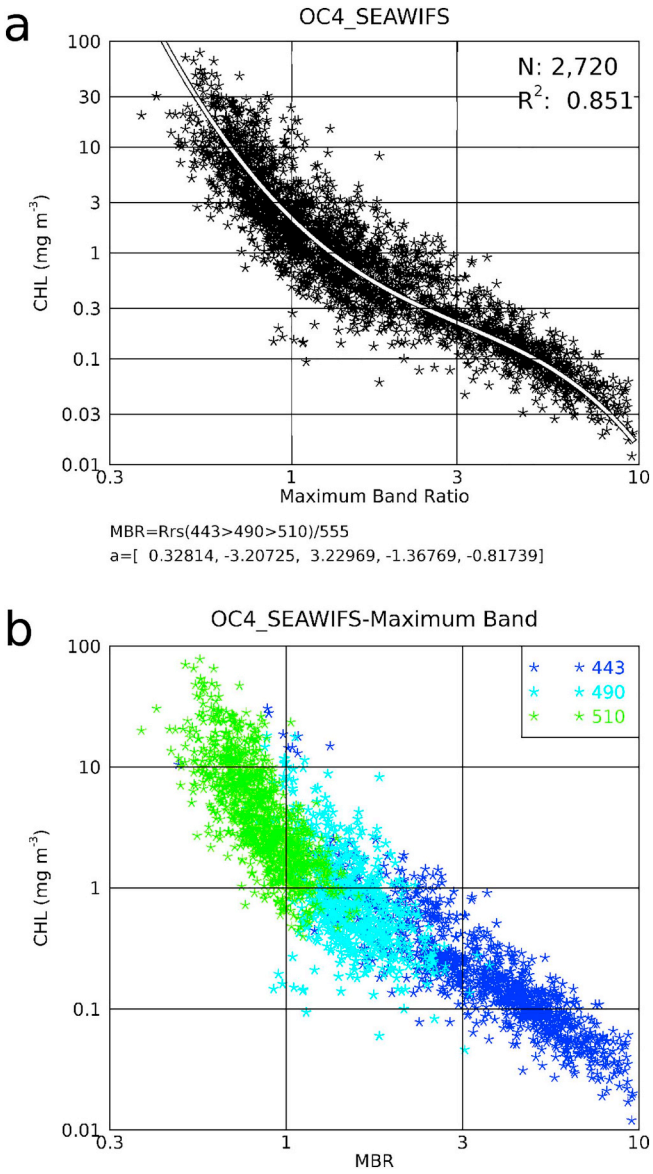

Fig. 3. OC4_SEAWIFS MBR CHL algorithm. (a) The asterisks represent the measured *in situ* data and the continuous curve represents the model. The fourth-order polynomial coefficients and bands used in the MBR equation are also shown. (b) Same as (a), but color coded to indicate the band used in the numerator of the MBR. (For interpretation of the references to color in this figure legend, the reader is referred to the web version of this article.)

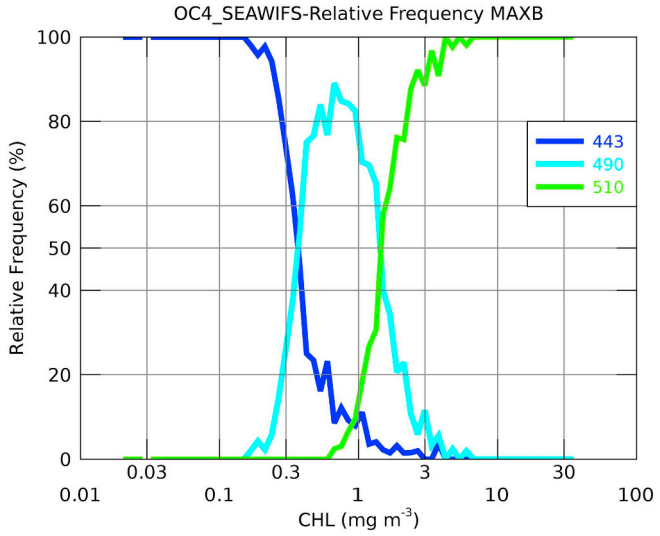

Fig. 4. The relative frequency of the dominant band used in the OC4_SEAWIFS model.

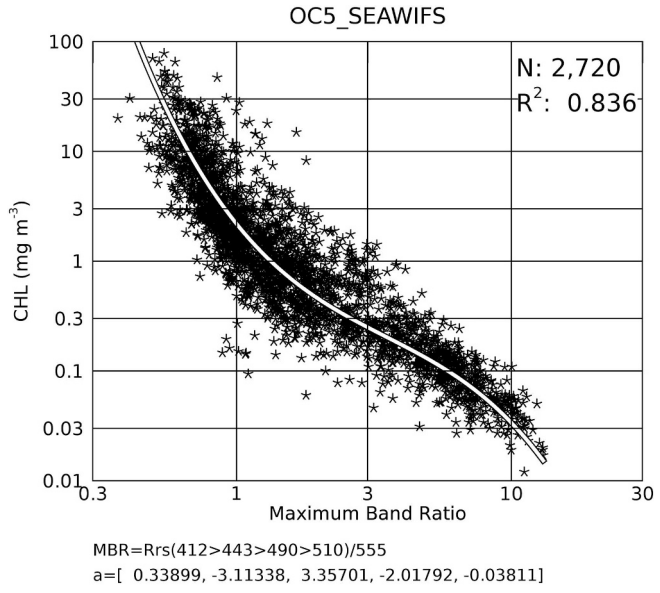

Fig. 5. OC5_SEAWIFS MBR CHL algorithm. The asterisks represent the measured *in situ* data and the continuous curve represents the model. The fourth-order polynomial coefficients and bands used in the MBR equation are also shown.

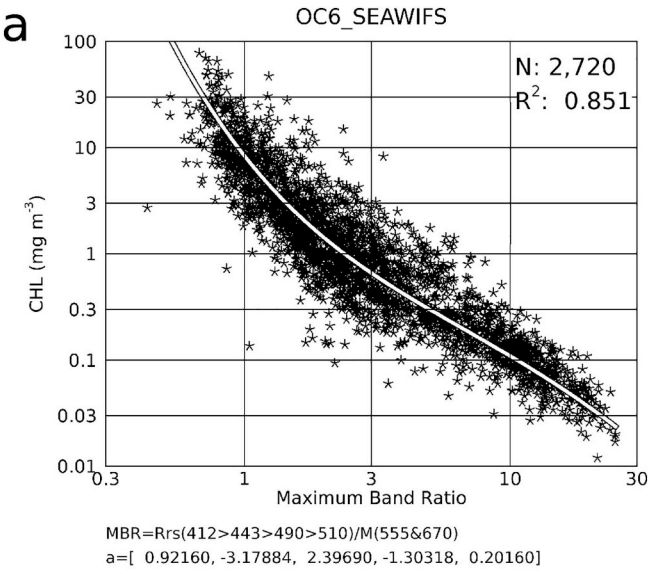

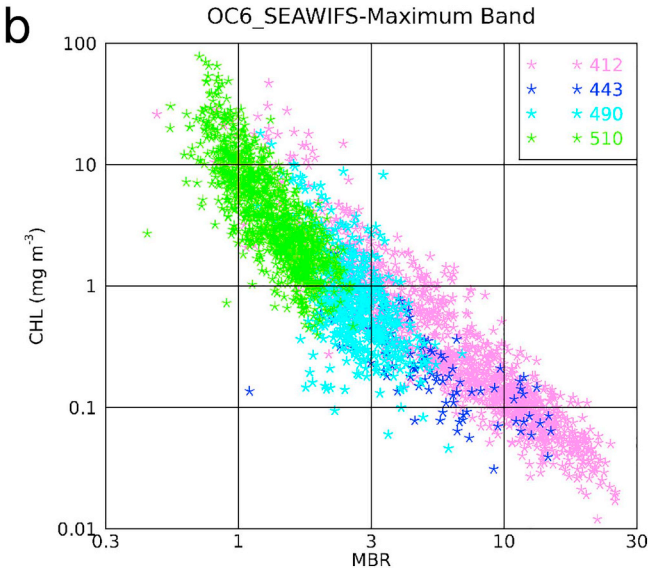

Fig. 6. OC6_SEAWIFS MBR CHL algorithm. (a) The asterisks represent the measured *in situ* data and the continuous curve represents the model. The fourth-order polynomial coefficients and bands used in the MBR equation are also shown. Note that M(555&670) indicates the use of the mean of Rrs_{555} and Rrs_{670}. (b) Same as (a), but color coded to indicate the band used in the numerator of the MBR. (For interpretation of the references to color in this figure legend, the reader is referred to the web version of this article.)

MBR. Table 7 lists algorithms having the same combinations of bands. The typically sigmoid shapes of the unique 43 MBR algorithms are portrayed in Fig. 9. Maximum band ratios progressively increase from the OC3 series to the OC6 series, that is, an increasing number of wavelengths are considered in the numerator with attendant decreases in Rrs in the denominators of the MBRs. Most of these curves exhibit a characteristic sigmoid relationship between band ratios and CHL in log-log space (O'Reilly et al., 1998; Fig. 11 of Valente and 42 co-authors, 2015). The most linear of these, OC6_GOCI, uses the longest wavelength-bands $RRS_{660\&680}$ in the denominator of the MBR (Table 6).

3.5. Algorithm consistency

A high degree of internal consistency among algorithms is an important prerequisite for merging data from multiple sensors. Excellent agreement and internal consistency exist across the 43 unique MBR algorithms. We compared model output from each unique MBR algorithm against all other algorithms, which totaled 903 combinations. In these 903 pairwise comparisons, 95% of the R^2 exceeded 0.853, and 90% of the regression slopes, approximately 1.0, were between 0.982 and 0.985 (Table 8). This consistency compares well with previous algorithm development activities (*e.g.*, https://oceancolor.gsfc.nasa.gov/atbd/chlor_a/) and offers some verification of our chosen fitting routine, particularly given the diversity of shapes and steepnesses across the full suite of OC algorithm forms (Fig. 9).

3.6. Algorithm validation - matchups with in situ data

A critical feature of CHL algorithms is their efficacy in retrieving satellite-derived estimates that agree well with *in situ* measurements. We obtained coincident Level-2 satellite-to-*in situ* CHL match-ups from the OBPG for SeaWiFS and MODIS-Aqua. All satellite data were

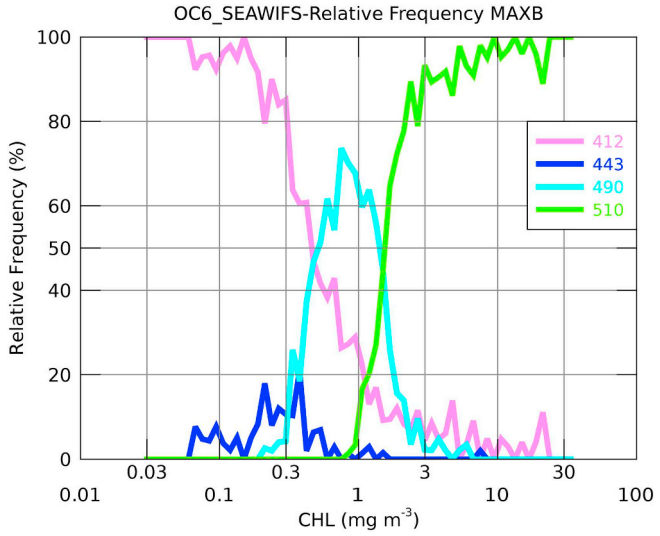

Fig. 7. The relative frequency of the dominant band used in the OC6_SEAWIFS model.

processed using their latest 2018 reprocessing configurations and satellite data post-processing followed the methods and exclusion criteria of Bailey and Werdell (2006). We consider three performance metrics following Seegers et al. (2018). First, we calculated median absolute error (MAE) as:

$$MAE = 10\text{^}\left(\frac{\sum_{i=1}^{n} |\log_{10}(\text{satellite}) - \log_{10}(in\ situ)|}{n}\right), \quad (4)$$

where n is the sample size, and bias as:

$$bias = 10\text{^}\left(\frac{\sum_{i=1}^{n} \log_{10}(\text{satellite}) - \log_{10}(in\ situ)}{n}\right), \quad (5)$$

Note that observations are log-transformed such that MAE and bias presents multiplicative metrics (that is, a MAE of 1.5 indicates that the satellite observations are 1.5× (50% greater) on average than the *in situ* observations). Finally, we generated pair-wise comparisons of the match-up pairs following the methods described in Seegers et al. (2018) to calculate the percentage of best performance (hereinafter referred to as "percent wins%") for each model. Table 9 summarizes results of the MAE and bias statistical comparisons, as well as percent wins% compared to the OCI algorithm currently employed by NASA. OCI uses the Hu et al. (2012) CI for CHL $< 0.15\,mg\,m^{-3}$, an OC Version -6 approach for CHL $> 0.2\,mg\,m^{-3}$ and a weighted blend of the two for the transition zone that spans $0.15 \leq CHL \leq 0.2\,mg\,m^{-3}$.

SeaWiFS and MODIS-Aqua Version -7 match-up results compare favorably with the existing implementation of OCI. Broadly speaking, all algorithms perform equivalently with regard to absolute biases. All SeaWiFS biases fall below 5.5% with the largest difference between algorithms (OCI and OC6) spanning only 2.9%. MODIS-Aqua biases rise to a range of 10.2 to 18.5% partially due to the reduced sample size and lower temporal and spatial variability relative to SeaWiFS. The SeaWiFS OCI bias, for example, rises from 2.6 to 8.2% when considering only match-ups from the MODIS-Aqua era. OC6 exhibits the lowest bias for MODIS-Aqua but also the only negative bias relative to *in situ* data (recall that a value less than unity indicates a negative bias). Match-up biases stem partially from the radiometric quality of the satellite instrument. For example, MODIS-Aqua Rrs satellite-to-*in situ* match-ups (see https://seabass.gsfc.nasa.gov) report positive biases for satellite Rrs_{412} and Rrs_{443} and negative biases for satellite Rrs_{547} and Rrs_{667} relative to *in situ* data. This positive bias in the numerator and negative bias in the denominator results in elevated satellite MBRs relative to *in situ* MBRs and, thus, reduced CHL estimates from an OC algorithm (Figs. 3, 5, and 6). When considering only $CHL \leq 0.2\,mg\,m^{-3}$, the SeaWiFS sample size falls to 439 and its biases rise to span a range of 28% for OC5 to 45% for OCI. When considering only $CHL > 0.2\,mg\,m^{-3}$, the SeaWiFS biases become 4.4%, 2.3%, 2.2%, and 1% for OCI, OC4, OC5, and OC6, respectively. Given that OCI employs OC4 Version -6 in this CHL range, these results suggest that the Version -7 algorithms improve upon biases relative to their earlier versions.

All algorithms also perform similarly with regards to MAE. The largest difference between all SeaWiFS and all MODIS-Aqua MAEs span 6.3 and 9.1%, respectively. This equates roughly to a ~4% difference on average between MAEs for each instrument and suggests common variability across algorithms. When considering only $CHL \leq 0.2\,mg\,m^{-3}$ or $CHL > 0.2\,mg\,m^{-3}$, SeaWiFS MAEs remain largely unchanged, spanning 58% for OCI to 67% for OC6 and 65% for OCI to 72% for OC5, respectively. For these two CHL ranges, MODIS-Aqua MAEs spanned 48% for OCI to 57% for OC6 and 66% for OC4 to 76% for OC6, respectively. No exceptional superiority emerges with regards to percent wins% when considering the full dynamic range of CHL. For SeaWiFS, OCI more closely matched *in situ* CHL than OC5 and OC6 for 58.5 and 55.3% of the satellite-to-*in situ* pairs respectively, and OC4 more closely matched *in situ* CHL than OCI for 51.4% of these pairs. MODIS-Aqua demonstrated similar results with OCI more closely matching *in situ* CHL than OC4 and OC6 for 56.8 and 59.5% of satellite-to-*in situ* pairs, respectively, and OC3 more closely matching *in situ* CHL than OCI for 51.6% of these pairs. When considering only $CHL > 0.2\,mg\,m^{-3}$, the OC4, OC5, and OC6 Version -7 approaches more closely matched *in situ* CHL than their Version -6 counterparts for > 97% of the satellite-to-*in situ* pairs for SeaWiFS and for > 99% for MODIS-Aqua, which again suggests that the Version -7 algorithms improve upon their earlier versions.

On average and in relative terms, OCI-derived CHL differed from that of SeaWiFS OC6, OC5, and OC4 by 16.4, 11.5, and 9.5% respectively, and from that of MODIS-Aqua OC6, OC4, and OC3 by 37.3, 13.2, and 9.7% respectively. The elevated difference for OC6_MODIS is expected given the magnitude of the difference in satellite-to-*in situ* match-up biases for the two algorithms, namely the positive bias (1.185) for OCI compared to the negative bias (0.899) for OC6_MODIS-Aqua (Table 9). When only considering $CHL \leq 0.2\,mg\,m^{-3}$, OCI-derived CHL differed from that of SeaWIFS OC6, OC5, and OC4 by 20.4, 19.4, and 18.2%, respectively, and from that of MODIS-Aqua OC6, OC4, and OC3 by 17.3, 15.0, and 17.7%, respectively, on average. In this CHL range, recall that these percentages translate roughly to only $0.02\,mg\,m^{-3}$ in absolute terms ($0.2 * 0.1\,mg\,m^{-3} = 0.02\,mg\,m^{-3}$).

4. Discussion

We developed 65 Version -7 OC algorithms for 25 satellite instruments using a global *in situ* dataset that, to our knowledge, represents the widest diversity of marine bio-optical conditions available at this time. Our motivation was to ensure that the next generation of this well-established and widely-adopted OC approach: (1) consider the most modern dataset possible and represent the largest dynamic range of ocean color water types; (2) extend to additional satellite instruments, including those for upcoming missions, with robust internal consistency across missions, and, (3) revisit the potential use of additional spectral information given improvements in atmospheric correction and instrument calibration and characterization that previously limited the confidence in the use of the bluest or red wavelengths. Ultimately, we believe that the Version -7 OC algorithms better represent global spatial and temporal bio-optical diversity than their predecessors, with increased information content through the use of a modern training dataset and the consideration of additional wavelengths.

Including additional satellite instruments and achieving internal consistency across missions offers several obvious advantages. First, the

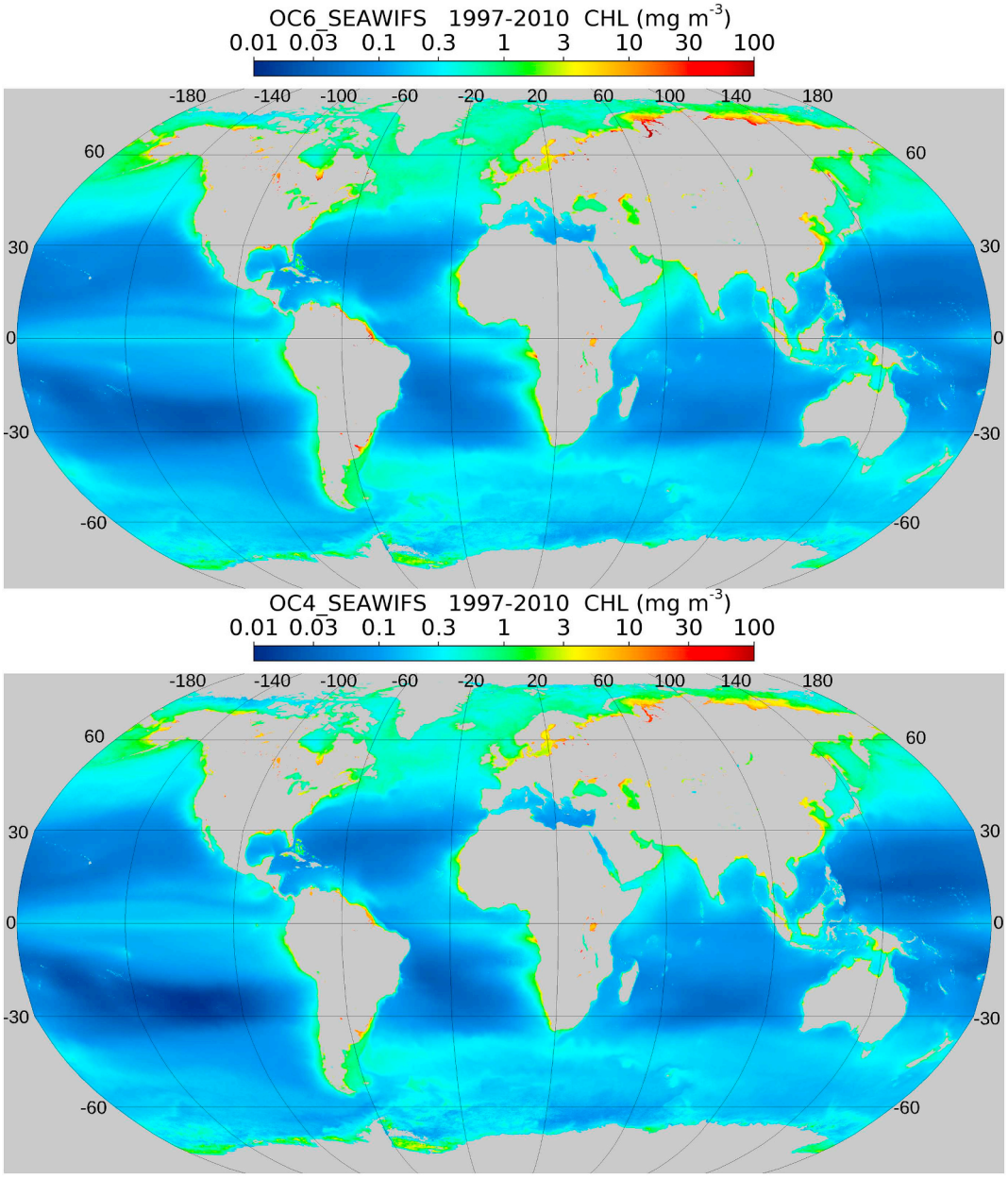

Fig. 8. Global distribution of CHL from the (upper) OC6_SEAWIFS and (lower) OC4_SEAWIFS models. These are based on all Rrs data available during the SeaWiFS

Table 7
Algorithms that use the same set of bands (center wavelengths).

N	Wavelengths	Algorithms
3	443;490;565	OC3_POLDER; OC3_POLDER_2;OC3_SGLI
7	443;490;510;555	OC4_SEAWIFS; OC4_HAWKEYE; OC4_OCI; OC4_OCM; OC4_OSMI; OC4_PACE_OCI; OC4_SABIA_MAR
6	412;443;490;510;555	OC5_SEAWIFS; OC5_HAWKEYE; OC5_OCM; OC5_OSMI; OC5_PACE_OCI; OC5_SABIA_MAR
3	412;443;490;510;555;670	OC6_SEAWIFS; OC6_HAWKEYE; OC6_OSMI
2	443;565	OC2_POLDER; OC2_POLDER_2
3	443;490;520;565	OC4_COCTS; OC4_GLI; OC4_MERSI
3	412;443;490;520;565	OC5_COCTS; OC5_GLI; OC5_MERSI

quality of merged CHL data products from multiple overlapping ocean color missions will improve. Such mergers remain critical for maximizing spatial and temporal coverages of the open ocean (Table 1) (IOCCG, 2007). Second, the expanded suite of Version -7 algorithms will provide an improved opportunity to link consistently ocean color satellite time-series from CZCS (1978) through the upcoming PACE mission (scheduled for launch in 2022) and beyond. Conceptually, this could stretch the climate data record of CHL to upwards of fifty years, offering an unprecedentedly consistent data set for the assessment of climate change. Many upcoming ocean color instruments include wavelength bands that will facilitate CHL retrievals through alternative approaches. For example, the inclusion of wavelengths shorter than 412 nm should be more effective in resolving CDOM from CHL than is currently possible within the remote sensing paradigm (McClain, 2009) since they will be farther away from the CHL absorption peak and more coincident with the region of strongest CDOM absorption. Several of the newer planned and recently launched ocean color sensors (will) have wavelength bands with centers < 412 nm, such as PACE, OLCI, and SGLI. This notwithstanding, our modernization of a heritage approach remains critical to ensure climate data record consistency as far back in time as possible.

While the use of violet (*e.g.*, 412 nm) and red (*e.g.*, 670 nm) bands

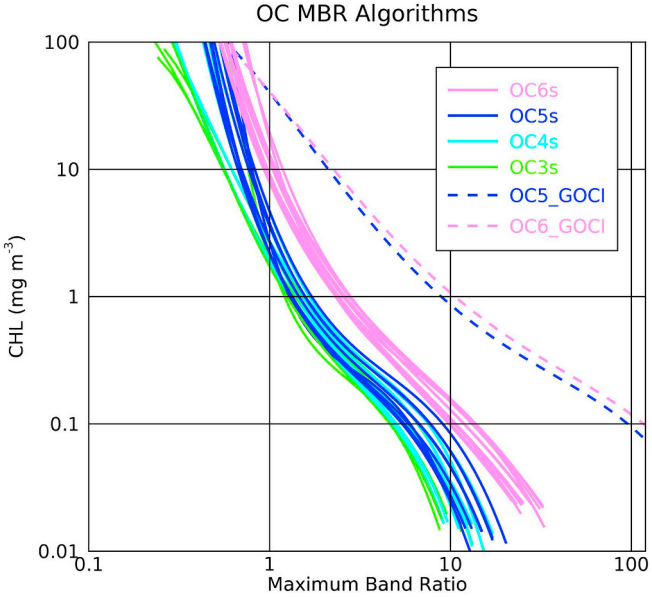

Fig. 9. Maximum band ratio *versus* CHL for 43 unique OC algorithms. Green indicates a 3-band MBR, cyan a 4-band MBR, blue a 5-band MBR, and violet a 6-band MBR. (For interpretation of the references to color in this figure legend, the reader is referred to the web version of this article.)

Table 8
Percentiles for the R^2 and slopes from 903 Reduced Major Axis linear regressions of all possible pairings of log-transformed CHL from the forty-three unique MBR algorithms. For the columns, % indicate percentiles, with the median value = 50%.

STAT	N	5%	25%	50%	75%	95%
R^2	903	0.853449	0.858966	0.858966	0.858966	0.859563
SLOPE	903	0.982403	0.984346	0.984516	0.984922	0.984977

Table 9
Relative performance of several Version -7 OC algorithms *versus* OCI as currently implemented by NASA. % Wins is presented relative to OCI.

Algorithm	N	Bias	MAE	% Wins
OCI_SEAWIFS	2278	1.02610	1.64047	
OC6_SEAWIFS	2278	1.05544	1.69528	44.6005
OC5_SEAWIFS	2278	1.02991	1.70390	41.5277
OC4_SEAWIFS	2278	1.03313	1.65678	51.4486
OCI_MODIS	955	1.18456	1.67799	
OC6_MODIS	955	0.89861	1.73929	40.5236
OC4_MODIS	955	1.14990	1.73111	43.1414
OC3_MODIS	955	1.17567	1.64796	51.6230

increases the dynamic range of MBR in oligotrophic water (thus, in a way, increasing the signal-to-noise of the algorithm), they have not previously been considered for routine use in OC algorithms. A known potential shortcoming of any MBR algorithm is its requirement for accurate radiometric calibration and internal consistency across three (OC3) to six (OC6) bands in lieu of a simpler two-band algorithm (OC2). For example, SeaWiFS radiometric calibrations were not sufficiently characterized at the time of its launch and, as such, NASA opted to use a two-band algorithm instead of a better performing (compared to *in situ* data) four-band MBR algorithm. Early in the mission, before the accuracy of and temporal stability in SeaWiFS radiometry were well characterized, nearly 25% and 7% of the retrievals of Rrs_{412} and Rrs_{443} respectively, were negative in phytoplankton-rich continental shelf water (O'Reilly and Yoder, 2003). Such negative retrievals also indicate atmospheric over-correction of retrieved Rrs for all bands which would have led to incorrect CHL estimates if not flagged during processing. Despite this, pre-launch instrument characterizations, on-orbit calibrations and atmospheric correction methods have all immensely improved in the two decades since SeaWiFS launched making the time right to start revisiting the use of Rrs_{412} and Rrs_{670} in OC algorithms.

We developed seventeen OC5 and eighteen OC6 CHL algorithms that include a violet band in the numerator of the MBR with wavelengths ranging between 408 and 416 nm. The denominators of the algorithms using only a green band in the denominator range from 553 to 660 nm (hereafter referred to as OC5 algorithms for convenience, despite several OC4 algorithms meeting this criterion), whereas the effective denominators of the OC6 algorithms that consider both green and red bands in the denominator range from 592.5 to 670 nm (Table 6). Broadly speaking, the Version -7 algorithms all perform similarly when comparing model output to *in situ* CHL. With regard to those with additional wavelengths, the OC6 algorithms may perform better than their OC5 counterparts because the effective wavelength of the average of the two Rrs in the MBR denominator resides on the relatively flat portion of the CHL absorption spectrum away from the secondary CHL absorption peak and farther away from the exponentially decreasing adg(λ) than one green Rrs alone. Validation of SeaWiFS and MODIS-Aqua CHL retrievals indicates similar statistical performance across the Version -7 algorithms and OCI for a global match-up dataset with almost four orders-of-magnitude in *in situ* CHL. This, however, makes it difficult to recommend the unequivocal use of one algorithm over the others and indicates that, perhaps, the inclusion of violet and red Rrs does not offer a remarkable improvement over existing blue-green algorithms. Rather, we adopt the philosophy put forward in Seegers et al. (2018) and recommend that individuals evaluate the performance of various CHL algorithms in their region of study (*e.g.*, selecting the approach that offers the best agreement with regional *in situ* CHL and best spatial or temporal coverage) and/or pursue educated decisions based on local knowledge or regional needs (*e.g.*, selecting OC4 *versus* OC5 *versus* OC6 based on expertise of instrument radiometric performance and/or CDOM-CHL covariance in a region of study). We offer the Version -7 algorithms with the hope that this large suite of approaches encompasses the most possible needs for the largest possible audience. While algorithms presented here are primarily intended for application at a global ocean scale, 'global' algorithms such as OC4_SEAWIFS have also assisted regional researchers in developing and evaluating regionally-specific chlorophyll algorithms. Global algorithms often act as benchmark-references with which to demonstrate potential improvements that regional algorithms may yield over the global algorithm. Some examples include Darecki and Stramski (2004), Garcia et al. (2005), D'Ortenzio et al. (2002), and Siswanto et al. (2011).

4.1. Additional considerations on use of a violet band

As previously stated, the violet band (412 nm) has rarely seen use in empirical CHL algorithms during the past forty years of ocean color research, driven in part by poor post-launch radiometric performance of violet and blue bands. In that time, conventional wisdom evolved to argue against consideration of Rrs_{412} in CHL algorithms, as knowledge of bio-optics and the relationships between CDOM and CHL improved. With this in mind, we realize some readers will view the consideration of Rrs_{412} in an MBR algorithm as controversial. Despite this, while rederiving coefficients for existing OC2, OC3, and OC4 band forms, we felt it would be a disservice to not test and evaluate the approach with increased spectral information to determine if Rrs_{412} (and Rrs_{670}) offer useful information and/or improve upon heritage approaches (which would certainly support the long effort to improve on-orbit instrument calibrations and atmospheric correction approaches). If anything, this might stimulate renewed discussion of such conventional wisdom in light of this work and other meaningful studies (*e.g.*, Siegel et al., 2002, Siegel et al., 2005b, Hu et al., 2006, Morel, 2009, to name only a few).

Additionally, SAA approaches that independently consider CDOM and CHL in some cases failed to improve upon empirical CHL retrievals (*e.g.*, Brewin et al., 2015), and we felt that consideration of Rrs_{412} and Rrs_{670} in the Version -7 algorithms could contribute to unraveling that conundrum.

We ultimately believed it timely to revisit the use of Rrs_{412} in empirical CHL algorithms given the useful knowledge it carries about chlorophyll *a* absorption in oligotrophic waters (the only areas where Rrs_{412} will be used in the MBR numerator). As previously stated, we also contend that the time is right to revisit and explore its use given improvements in instrument characterization and advances in atmospheric correction methods that previously precluded its consideration. It is well understood that CDOM absorption decreases approximately exponentially with increasing wavelengths and that its spectrum overlaps with the chlorophyll absorption spectrum at wavelengths between 400 and 600 nm (*e.g.*, Bricaud et al., 1981). It is also well known that CDOM absorption can strongly influence the Rrs_{412} retrieval (Siegel et al., 2002; Siegel et al., 2005a; Siegel et al., 2005b). Per Bricaud et al. (1998), chlorophyll *a* has a very broad absorption spectrum with a primary absorption peak at 443 nm, a secondary peak at 673 nm and minimum absorption around 570 nm (Fig. 10). Most ocean color sensors include a band centered in the blue region of the spectrum at ~443 nm (see Table 2) and, therefore, capture the peak of chlorophyll *a* absorption. Consequently, the 443 nm band has been regarded as the primary chlorophyll-detecting band in the passive remote sensing paradigm. Rrs_{412} has often been used in CDOM algorithms, but infrequently in empirical CHL algorithms. However, absorption by CHL at 412 nm is 71.3% of the peak absorption at 443 nm (Fig. 10), and nearly one third (31.3%) of the total CHL-specific absorption between 400 and 700 nm occurs below 443 nm in the blue-violet region, both of which suggest that bands below 443 nm (*e.g.*, the 412 nm present on most heritage instruments) can be useful in detecting chlorophyll in regions where the assumption of CHL and CDOM covariation remains valid.

We offer the following for future consideration regarding the use of Rrs_{412} in an MBR algorithm. First, Table 3 empirically demonstrates that Rrs_{412}:Rrs_{555} and Rrs_{443}:Rrs_{555} *versus in situ* CHL have comparable R^2 for the clearest waters in the Valente dataset. This indicates responsiveness of Rrs_{412} to changes in chlorophyll concentration, despite the overlapping CDOM absorption spectra. Second, the empirical OC algorithms that include Rrs_{412}, such as OC5_SEAWIFS and OC6_SEAWIFS, have comparable R^2 for MBR *versus in situ* CHL (0.836 and 0.851, respectively) with those not using Rrs_{412}, such as OC4_SEAWIFS (0.851). Note, the global distribution of CHL from the OC6_SEAWIFS algorithm, based on the entire SeaWiFS mission dataset, is generally similar to the distribution from OC4_SEAWIFS (Fig. 8). Third, SeaWiFS and MODIS-Aqua satellite-to-*in situ* match-ups show comparable results in waters with CHL $< 0.2\,mg\,m^{-3}$ when including and not including Rrs_{412}. Biases and MAEs for OC4_, OC5_, and OC6_SEAWIFS are 31, 28, and 38% and 60, 64, and 67%, respectively. Biases and MAEs for OC3_, OC4_, and OC6_MODIS are 43, 36, and 40% and 56, 54, and 57%, respectively (noting that OC4_MODIS includes Rrs_{412} in its numerator). Finally, the inclusion of Rrs_{412} in the MBR numerator extends its dynamic range such that retrieved CHL are less sensitive to uncertainties in MBR. As a demonstration of this, consider that corresponding MBRs for OC4_, OC5_, and OC6_SEAWIFS for CHL = $0.1\,mg\,m^{-3}$ are approximately 5.0, 5.9, and 10.6, respectively. Changing the MBRs by −10, −5, −2, 2, 5, and 10% corresponds to changes in retrieved CHL from OC4_SEAWIFS by 20, 9.5, 3.7, −3.6, −8.7, and −16.7%, respectively. These changes in CHL fall to 17.6, 8.4, 3.3, −3.1, −7.6, −14.6%, respectively, for OC5_SEAWIFS and to 17.0, 8.0, 3.1, −2.9, −7.1, and − 13.5%, respectively, for OC6_SEAWIFS.

4.2. Frequency distribution of the maximum band (MaxB) and trophic status

Finally, the concept of MBR itself offers what we believe to be a reliable proxy indicator for the trophic status of a body of water. The terms 'oligotrophic,' 'mesotrophic' and 'eutrophic' (meaning well-nourished) get frequent use in the scientific literature to designate trophic status, however, quantitative definitions in terms of CHL levels are arbitrarily defined. The OBPG, for example, builds on the CZCS analyses of Antoine et al. (1996) by defining oligo-, meso-, and eutrophic as CHL $\leq 0.1\,mg\,m^{-3}$, $0.1 <$ CHL $< 1.0\,mg\,m^{-3}$, and CHL $\geq 1\,mg\,m^{-3}$ respectively in their reporting. We contend that the frequency of the brightest, maximum band (MaxB) in the MBR of the OC6_SEAWIFS algorithm, may serve as a useful, reproducible, bio-optically-based index of trophic status. To that end, we pursued the following to assess the widely adopted boundaries of 0.1 and $1.0\,mg\,m^{-3}$ and to explore a simple bio-optical resource for further evaluating regional and global changes in aquatic biogeochemistry (*e.g.*, changing distributions of MaxB indicate changes in aquatic optical properties).

The frequency distribution of the maximum band based on all the available daily SMI Rrs(λ) data from the SeaWiFS mission is illustrated in Fig. 11. To generate this distribution, we identified the maximum band (MaxB) of Rrs_{412}, Rrs_{443}, Rrs_{490} and Rrs_{510} for each pixel in each SMI image encompassing the mission duration, 1997–2010. The overlap among bands is similar to the overlap in the *in situ* data for OC6_SEAWIFS (Fig. 7), but the frequency curves are much smoother because the mission dataset (2,058,929,408) is so much larger than the *in situ* dataset (2720). Rrs_{412} generally prevails over other bands from the lowest CHL to $\sim 0.5\,mg\,m^{-3}$, after which Rrs_{490} begins its dominance. The transition from dominance by Rrs_{490} to Rrs_{510} begins at a CHL of $\sim 1.67\,mg\,m^{-3}$, above which Rrs_{510} generally dominates. When we examined the long-term-mission means for SeaWiFS Rrs data, we found that the median CHL values for the regions where the means for Rrs_{412}, Rrs_{443}, Rrs_{490}, and Rrs_{510} dominate are ~0.10, 0.34, 0.70, and $3.1\,mg\,m^{-3}$, respectively. The long-term mean for Rrs_{412} dominates other bands for much of the world ocean, with the Rrs_{412}:Rrs_{443} ratio exceeding unity for > 80% of valid pixel retrievals. But, Rrs_{412} and Rrs_{443} are not always strongly dissimilar. In those regions where the mean Rrs_{412} dominates, the 25th, 50th (median) and 75th percentiles of the Rrs_{412}:Rrs_{443} ratio are 1.14, 1.20, and 1.27, respectively. In those regions where the long-term mean Rrs_{443} dominates, the ratios at these percentiles are 0.93, 0.97, and 0.98, respectively.

We propose that the use of reproducible radiometry to define CHL thresholds provides a modern tool to define these definitions of trophic

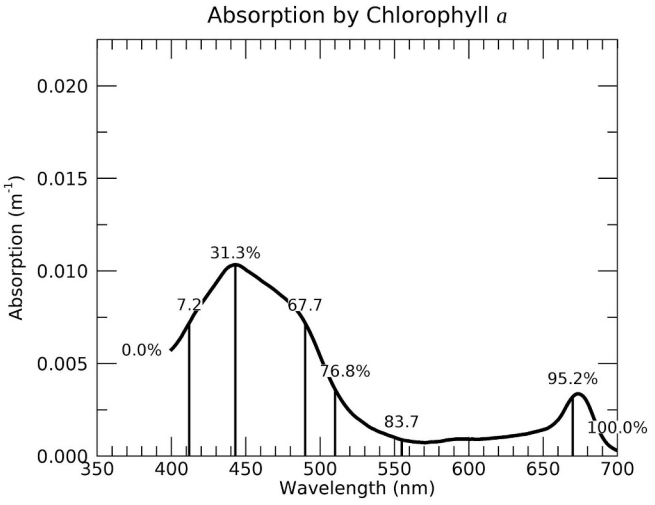

Fig. 10. Example absorption spectrum for phytoplankton chlorophyll *a*. The modeled phytoplankton absorption spectrum is based on equations from Bricaud et al. (1998) and the mean global CHL of $0.18\,mg\,m^{-3}$. The percent of the total cumulative absorption from 400 to 700 nm is also shown above the absorption spectrum, and the vertical lines below the curve intersect the x axis at the six wavelengths on the SeaWiFS sensor.

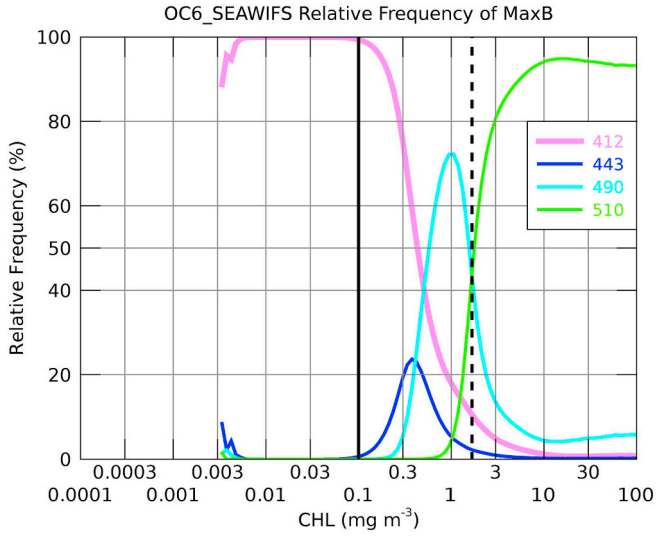

Fig. 11. Relative frequency distributions of MaxB, the dominant band in the OC6_SEAWIFS MBR based on all available daily (4502) SMI Rrs data from the SeaWiFS mission.

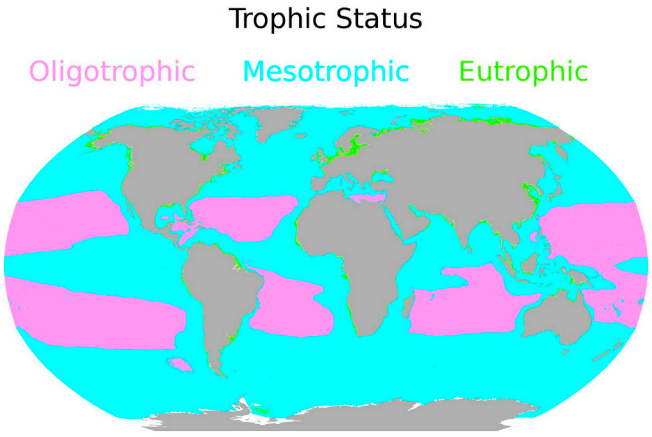

Fig. 12. Global map of trophic status using trophic status criteria in Fig. 11.

status, particularly to assess changes over time. At CHL less than ~0.1 mg m^{-3}, Rrs_{412} dominates nearly 100% of the time while at CHL above 1.67 mg m^{-3}, Rrs_{510} begins to dominate Rrs_{490} and all other bands. Between 0.1 and 1.67 mg m^{-3}, Rrs_{443}, Rrs_{490}, and Rrs_{510} share dominance with Rrs_{412} (Fig. 11). To tie a definition of trophic status to a modern satellite dataset and stimulate community discussion, we therefore propose that the solid vertical black line at 0.1 mg m^{-3} in Fig. 11 operationally defines the upper concentration of CHL in oligotrophic water while the dashed vertical black line at 1.67 mg m^{-3} operationally delineates the lowest CHL for eutrophic water. The region with CHL above 0.1 mg m^{-3} and below 1.67 mg m^{-3} is, therefore, considered as mesotrophic water. Application of these criteria to the 40-year SMI mean CHL for the global ocean (see Fig. 1), yields the percent of ocean area indexed as oligotrophic, mesotrophic and eutrophic as 24.25, 67.04, and 8.71%, respectively (Fig. 12). For comparison, Antoine et al. (1996) reported percent of ocean area indexed as olig-, meso- and eutrophic for the latitudinal band spanning 50°S to 50°N as 55.8%, 41.8%, and 2.4%, with the boundary between meso- and eutrophic defined at 1.0 mg m^{-3}. Fig. 12 clearly indicates that our mesotrophic and eutrophic regions expand into higher latitudes. Broadly speaking and not surprisingly, the oligotrophic regions shown in Fig. 12 follow the spatial patterns of open ocean gyres while the eutrophic areas remain mostly restricted to highly productive near-shore regions of continental shelves.

5. Concluding remarks

Community interest undeniably extends well beyond CHL to other geophysical measurements and, as previously stated, we anticipate the development of improved methods for retrieving CHL with the forthcoming increased spectral resolution of future satellite instruments. Nonetheless, maintenance of a suite of simple, sensor-to-sensor consistent, empirical OC algorithms remains worthwhile. We repeatedly highlighted their value in mission-merging activities and climate data record development. In addition, OC algorithms have routinely proven themselves useful for comparing and verifying the radiometric performances of overlapping ocean color missions (Franz et al., 2005; Franz et al., 2018). These global empirical algorithms have also served as performance references when developing and evaluating *in situ* data sets (Werdell and Bailey, 2005), regional algorithms (*e.g.*, Kahru and Mitchell, 2001; Carder et al., 2004; Werdell et al., 2009), and more complex SAA approaches (IOCCG, 2006; Werdell et al., 2018).

Through this work, we generated the most up-to-date suite of OC algorithms using the most spatially and temporally diverse *in situ* dataset available for the largest number of satellite instruments ever considered, with the long-term purpose of facilitating CHL climate data record development spanning four-plus decades. We also presented expanded versions of the OC algorithms that make use of additional spectral information when available (wavelengths on or near 412 and 670 nm). Our goals were to provide modern versions of this core algorithm that better represent spatial and temporal bio-optical diversity than their predecessors and to explore increasing information content through the inclusion of additional wavelengths. We further proposed to expand their utility to the definition of trophic status, which broadly reinforces previously suggested thresholds, but offers a more direct tie to aquatic biochemistry anchored to remote-sensing reflectances. We expect the continued use of the OC approach well into the future and, as such, offer the Version -7 algorithms as the next generation for use in CHL climate record development.

Acknowledgements

We thank C. R. McClain for his guidance to us and the ocean color community during the past three decades. We greatly appreciate the extensive efforts by A. Valente and his forty-two co-authors for assembling, maintaining, and quality-controlling a large globally-representative database of *in situ* chlorophyll, remote-sensing reflectances, and associated measurements. We thank three anonymous reviewers for their deeply insightful comments that greatly improved this manuscript. Finally, we thank J.C. Landry for editorial assistance and S. Maritorena for making available his IDL software. Support for this effort was provided through a NASA Ocean Biology and Biogeochemistry *The Science of Terra, Aqua, Suomi NPP* award.

References

Aiken, J., Moore, G., Trees, C., Hooker, S., Clark, D., 1995. SeaWiFS CZCS-Type pigment algorithm. NASA Tech Memo., vol. 29 104566. (34 pp.).
Antoine, D., Andre, J., Morel, A., 1996. Oceanic primary production: 2. Estimation at global scale from satellite (Coastal Zone Color Scanner) chlorophyll. Glob. Biogeochem. Cycles 10 (1), 57–69.
Bailey, S.W., Werdell, P.J., 2006. A multi-sensor approach for the on-orbit validation of ocean color satellite data produts. Remote Sens. Environ. 102, 12–23.
Behrenfeld, M.J., O'Malley, R.T., Siegel, D.A., McClain, C.R., Sarmiento, J.L., Feldman, G.C., Milligan, A.J., Falkowski, P.G., Letelier, R.M., Boss, E., 2006. Climate-driven trends in contemporary ocean productivity. Nature 444, 752–755.
Brewin, R., Mélin, F., Sathyendranath, S., Steinmetz, F., Chuprin, A., Grant, M., 2014. On the temporal consistency of chlorophyll products derived from three ocean-colour sensors. ISPRS J. Photogramm. Remote Sens. 97, 171–184.
Brewin, R.J.W., Sathyendranath, S., Muller, D., Brockmann, C., Deschamps, P.-Y., Devred, E., Doerffer, R., Fomferra, N., Franz, B., Grant, M., Groom, S., Horseman, A., Hu, C., Krasemann, H., Lee, Z.-P., Maritorena, S., Melin, F., Peters, M., Platt, T., Regner, P., Smyth, T., Steinmetz, F., Swinton, J., Werdell, J., White, I.I.I,.G.N., 2015. The Ocean Colour Climate Change Initiative: III. A round-robin comparison on in-water bio-optical algorithms. Remote Sens. Environ. 162, 271–294.

Bricaud, A., Morel, A., Prieur, L., 1981. Absorption by dissolved organic matter of the sea (yellow substance) in the UV and visible domains. Limnol. Oceanogr. 26, 43–53.
Bricaud, A., Morel, A., Babin, M., Allali, K., Claustre, H., 1998. Variations of light absorption by suspended particles with chlorophyll *a* concentrations in oceanic (Case 1) waters: analysis and implications for bio-optical models. J. Geophys. Res. 103, 31,033–31,044.
Carder, K.L., Chen, F., Cannizzaro, J., Campbell, J., Mitchell, B., 2004. Performance of the MODIS semi-analytical ocean color algorithm for chlorophyll-*a*. Adv. Space Res. 33, 1152–1159.
Claustre, H., Maritorena, S., 2003. The many shades of ocean blue. Science 302, 1514–1515.
Dall'Olmo, G., Gitelson, A., Rundquist, A., Leavitt, D., Barrow, B., Holz, J., 2005. Assessing the potential of SeaWiFS and MODIS for estimating chlorophyll concentration in turbid productive waters using red and near-infrared bands. Remote Sens. Environ. 96, 176−187.
Darecki, M., Stramski, D., 2004. An evaluation of MODIS and SeaWiFS bio-optical algorithms in the Baltic Sea. Rem. Sens. Environ. 89, 326–350. https://doi.org/10.1016/j.rse.2003.10.012.
Dierssen, H., 2010. Perspectives on empirical approaches for ocean color remote sensing of chlorophyll in a changing climate. Proc. Natl. Acad. Sci. 107 (40), 17073–17078.
Doerffer, R., Schiller, H., 2007. The MERIS Case 2 water algorithm. Int. J. Remote Sens. 28, 517–535.
D'Ortenzio, F., Marullo, S., Ragni, d'Alcala, M., Santoleri, R., 2002. Validation of empirical SeaWiFS algorithms for chlorophyll-*a* retrieval in the Mediterranean Sea: a case study for oligotrophic seas. RSE 79–94.
Franz, B.A., Werdell, P., Meister, G., Bailey, S.W., Eplee, R.E., Feldman, G.C., Kwiatkowska, G., McClain, C.R., Patt, F.S., Thomas, D., 2005. The continuity of ocean color measurements from SeaWiFS to MODIS. Proc. SPIE 5882. https://doi.org/10.1117/12.620069.
Franz, B.A., Karakoylu, E., Siegel, D., Westberry, T., 2018. Global ocean phytoplankton. In: State of the Climate 2017. Bulletin of the American Meteorological Society, pp. 594–596.
Garcia, C.A.E., Garcia, V.M.T., McClain, C.R., 2005. Evaluation of SeaWiFS chlorophyll algorithms in the Southwestern Atlantic and Southern Oceans. Rem. Sens. Environ. 95, 125–137.
Gilerson, A., Gitelson, A., Zhou, J., Gurlin, D., Moses, W., Ioannou, I., Ahmed, S., 2010. Algorithms for remote estimation of chlorophyll-*a* in coastal and inland waters using red and near infrared bands. Opt. Express 18, 24109–24125.
Gitelson, A., Schalles, J., Hladik, C., 2007. Remote chlorophyll-*a* retrieval in turbid, productive estuaries: Chesapeake Bay case study. Remote Sens. Environ. 109, 464–472 (doi: 10.1016).
Gordon, H.R., Wang, M., 1994. Retrieval of water-leaving radiance and aerosol optical thickness over the oceans with SeaWiFS: a preliminary algorithm. Appl. Opt. 33 (3), 443–452.
Gordon, H.R., Clark, D.K., Brown, J.W., Brown, O.B., Evans, R.H., Broenkow, W.W., 1983. Phytoplankton pigment concentrations in the Middle Atlantic Bight: comparison of ship determinations and CZCS estimates. Appl. Opt. 22, 20–36. https://doi.org/10.1364/AO.22.000020.
Gregg, W.W., Casey, N., 2007. Sampling biases in MODIS and SeaWiFS ocean chlorophyll data. Remote Sens. Environ. 111, 25–35.
Gregg, W.W., Woodward, R., 1998. Improvements in coverage frequency of ocean colour: combining data from SeaWiFS AND MODIS. IEEE Trans. Geosci. Remote Sens. 36 (4), 1350–1353.
Henson, S., Dunne, J., Sarmiento, J., 2009. Decadal variability in North Atlantic phytoplankton blooms. J. Geophys. Res. 114 (C4), C04013. https://doi.org/10.1029/2008JC005139.
Hirata, T., Hardman-Mountford, N., Brewin, J., Aiken, R., Barlow, J., Suzuki, R., et al., 2011. Synoptic relationships between surface chlorophyll-*a* and diagnostic pigments specific to phytoplankton functional types. Biogeosciences 8, 311–327. https://doi.org/10.5194/bg-8-311-2011.
Hu, C., Lee, Z., Muller-Karger, F.E., Carder, K.L., Walsh, J.J., 2006. Ocean color reveals phase shift between marine plants and yellow substance. IEEE Geoscience and Remote Sensing 3, 262–266.
Hu, C., Lee, Z., Franz, B.A., 2012. Chlorophyll algorithms for oligotrophic oceans: a novel approach based on three-band reflectance difference. J. Geophys. Res. 117, C01011. https://doi.org/10.1029/2011JC007395.
IOCCG, 2006. Remote sensing of inherent optical properties: fundamentals, tests of algorithms, and applications. In: Reports of the International Ocean-colour Coordinating Group No. 5. IOCCG, Dartmouth, Canada.
IOCCG, 2007. Ocean-colour data merging. In: Reports of the International Ocean-colour Coordinating Group, No. 6. IOCCG, Dartmouth, Canada.
IOCCG, 2009a. Remote sensing in fisheries and aquaculture. In: Reports of the International Ocean-colour Coordinating Group, No. 8. IOCCG, Dartmouth, Canada.
IOCCG, 2009b. Partition of the Ocean into Ecological Provinces: Role of Ocean-colour Radiometry. Reports of the International Ocean-colour Coordinating Group, No. 9, IOCCG, Dartmouth, Canada.
Kahru, M., Mitchell, B.G., 2001. Seasonal and nonseasonal variability of satellite-derived chlorophyll and coloured dissolved organic matter concentration in the California Current. J. Geophys. Res. 106 (C2), 2517–2529.
Kwiatkowska, E., Fargion, G., 2002. Merger of ocean color information from multiple satellite missions under the NASA SIMBIOS project office. Proceedings of the Fifth International Conference on Information Fusion 291–298. https://doi.org/10.1109/ICIF.2002.1021164.
Lee, Z.P., Wei, J., Voss, K., Lewis, M., Bricaud, A., Huot, Y., 2015. Hyperspectral absorption coefficient of "pure" seawater in the range of 350–500 nm inverted from remote sensing reflectance. Appl. Opt. 54, 546–558.
McClain, C.R., 2009. A decade of satellite ocean color observations. Annual Reviews of Marine Science 1, 19–42.
Melin, F., Sclep, G., 2015. Band shifting for ocean color multi-spectral reflectance data. Opt. Express 23, 2262–2279. https://doi.org/10.1364/OE.23.002262.
Mobley, C., Werdell, J., Franz, B., Ahmad, Z., Bailey, S., 2016. Atmospheric correction for satellite ocean color radiometry. In: NASA Tech. Memo, NASA/TM-2016-217551, pp. 85.
Morel, A., 1974. Optical properties of pure water and pure sea water. In: Jerlov, N., Steeman Nielsen, E. (Eds.), Optical Aspects of Oceanography. Academic, San Diego, California, pp. 1–24.
Morel, A., 2009. Are the empirical relationships describing the bio-optical properties of case 1 waters consistent and internally compatible? J. Geophys. Res. 114, C01016. https://doi.org/10.1029/2008JC004803.
Morel, A., Maritorena, S., 2001. Bio-optical properties of oceanic waters: a reappraisal. J. Geophys. Res. 106 (C4), 7163–7180.
Moses, W.J., Gitelson, A., Berdnikov, A., Saprygin, S., Povazhnyi, V., 2012. Operational MERIS-based NIR-red algorithms for estimating chlorophyll-*a* concentrations in coastal waters — the Azov Sea case study. Remote Sens. Environ. 121, 118–124. https://doi.org/10.1016/j.rse.2012.01.024.
NRC, 2011. Assessing Requirements for Sustained Ocean Color Research and Operations. National Academies Press.
O'Reilly, J.E., 2017. Status and Trends in Primary Productivity and Chlorophyll From 1996 to 2014 in Large Marine Ecosystems and the Western Pacific Warm Pool, Based on Data From Satellite Ocean Colour Sensors. Intergovernmental Oceanographic Commission Technical Series 120 UNESCO, Paris (130 pp.).
O'Reilly, J.E., Yoder, J., 2003. A comparison of SeaWiFS LAC products from the third and fourth reprocessing: Northeast US ecosystem. Chapter 10. In: Hooker, S.B., Firestone, E.R. (Eds.), Patt, F. et al., Algorithm Updates for the Fourth SeaWiFS Data Reprocessing, NASA Tech. Memo. 2003-206892. vol. 22. NASA Goddard Space Flight Center, Greenbelt, Maryland, pp. 60–67.
O'Reilly, J.E., Maritorena, S., Mitchell, G., Siegel, D., Carder, K., Garver, S., Kahru, M., McClain, C.R., 1998. Ocean color chlorophyll algorithms for SeaWiFS. J. Geophys. Res. 103, 24937–24953.
O'Reilly, J.E., Maritorena, S., O'Brien, M., Siegel, D., Toole, D., Menzies, D., Smith, R., Mueller, J., Mitchell, G., Kahru, M., Chavez, F., Strutton, P., Cota, G., Hooker, S., McClain, C., Carder, K., Muller-Karger, F., Harding, L., Magnuson, A., Phinney, D., Moore, G., Aiken, J., Arrigo, K., Letelier, R., Culver, M., 2000. Ocean color chlorophyll *a* algorithms for SeaWiFS, OC2, and OC4: Version 4. In: Hooker, S.B., Firestone, E.R. (Eds.), SeaWiFS Postlaunch Calibration and Validation Analyses, Part 3. NASA Tech. Memo. 2000-206892 11. NASA Goddard Space Flight Center, Greenbelt, pp. 9–23.
PACE Science Definition Team, 2018. Pre-Aerosol, Clouds, and Ocean Ecosystem (PACE) Mission Science Definition Team Report. NASA/TM- 2018-219027/. 2 Goddard Space Flight Center, Greenbelt, Maryland (274 pp.).
Pope, R.M., Fry, E.S., 1997. Absorption spectrum (380–700 nm) of pure water. II. Integrating cavity measurements. Appl. Opt. 36, 8710–8723.
Saba, V., Friedrichs, M., Antoine, D., Armstrong, R., Asanuma, I., Behrenfeld, M., Ciotti, A., Dowell, M., Hoepffner, N., Hyde, K., Ishizaka, J., Kameda, T., Marra, J., Melin, F., Morel, A., O'Reilly, J.E., Scardi, M., Smith, W., Smyth, T., Tang, S., Uitz, J., Waters, K., Westberry, T., 2011. An evaluation of ocean color model estimates of marine primary productivity in coastal and pelagic regions across the globe. Biogeosciences 8, 489–503.
Seegers, B.N., Stumpf, R.P., Schaeffer, B.A., Loftin, K.A., Werdell, P.J., 2018. Performance metrics for the assessment of satellite data products: an ocean color case study. Opt. Express 26. https://doi.org/10.1364/OE.26.007404.
Siegel, D.A., Maritorena, S., Nelson, N.B., Hansell, D.A., Lorenzi-Kayser, M., 2002. Global distribution and dynamics of colored dissolved and detrital organic materials. J. Geophys. Res. 107 (C12), 3228. https://doi.org/10.1029/2001JC000965.
Siegel, D.A., Maritorena, S., Nelson, N.B., Behrenfeld, M.J., McClain, C.R., 2005a. Colored dissolved organic matter and its influence on the satellite-based characterization of the ocean biosphere. Geophys. Res. Lett. 32, L20605. https://doi.org/10.1029/2005GL024310.
Siegel, D.A., Maritorena, S., Nelson, N.B., Behrenfeld, M.J., 2005b. Independence and interdependencies among global ocean color properties: reassessing the bio-optical assumption. J. Geophys. Res. 110, C07011. https://doi.org/10.1029/2004JC002527.
Siegel, D.A., Behrenfeld, M., Maritorena, S., McClain, C., Antoine, D., Bailey, S., Bontempi, P., Boss, E., Dierssen, H., Doney, S., Eplee, R., Evans, R., Feldman, G., Fields, E., Franz, B., Kuring, N., Mengelt, C., Nelson, N., Patt, F., Robinson, W., Sarmiento, J., Swan, C., Werdell, P., Westberry, T., Wilding, J., Yoder, J., 2013. Regional to global assessment of phytoplankton dynamics from the SeaWiFS mission. Remote Sens. Environ. 135, 77–91.
Siswanto, E., Tang, J., Yamaguchi, H., Ahn, Y., Ishizaka, J., Yoo, S., Kim, S., Kiyomoto, Y., Yamada, K., Chiang, C., Kawamura, H., 2011. Empirical ocean-color algorithms to retrieve chlorophyll-*a*, total suspended matter, and colored dissolved organic matter absorption coefficient in the Yellow and East China Seas. J. Oceanogr. 67, 627–650.
Uitz, J., Claustre, H., Gentili, B., Stramski, D., 2010. Phytoplankton class-specific primary production in the world's oceans: seasonal and interannual variability from satellite observations. J. Geophys. Res. 24, GB3016. https://doi.org/10.1029/2009GB003468o.
Valente, A., et al., 2015. A compilation of global bio-optical in situ data for ocean-colour satellite applications. doi:10.1594/PANGAEA.854832, Supplement to: Valente, A., Sathyendranath, S., Brotas, V., Groom, S., Grant, M., Taberner, M., Antoine, D., Arnone, R., Balch, W., Barker, K., Barlow, R., Bélanger, S., Berthon, J., Besiktepe, S., Brando, V., Canuti, E., Chavez, F., Claustre, H., Crout, R., Frouin, R., García-Soto, C., Gibb, S., Gould, R., Hooker, S., Kahru, M., Klein, H., Kratzer, S., Loisel, H., McKee, D., Mitchell, B., Moisan, T., Muller-Karger, F., O'Dowd, L., Ondrusek, M., Poulton, A.,

Repecaud, M., Smyth, T., Sosik, H., Twardowski, M., Voss, K., Werdell, J., Wernand, M., Zibordi, G., (2016): a compilation of global bio-optical in situ data for ocean-colour satellite applications. Earth System Science Data 8 (1), 235–252.

Werdell, P.J., Bailey, S., 2005. An improved in-situ bio-optical data set for ocean color algorithm development and satellite data product validation. Remote Sens. Environ. 98, 122–140.

Werdell, P.J., Bailey, S., Franz, B., Harding, L., Feldman, G., McClain, C., 2009. Regional and seasonal variability of chlorophyll-*a* in Chesapeake Bay as observed by SeaWiFS and MODIS-Aqua. Remote Sens. Environ. 113, 1319–1330.

Werdell, P.J., Franz, B.A., Bailey, S.W., Feldman, G.C., Boss, E., Brando, V., Dowell, M., Hirata, T., Lavender, S., Lee, Z., Loisel, H., Maritorena, S., Mélin, F., Moore, T., Smyth, T., Antoine, D., Devred, E., d'Andon, O., Mangin, A., 2013. Generalized ocean color inversion model for retrieving marine inherent optical properties. Appl. Opt. 52 (10), 2019–2037.

Werdell, P.J., McKinna, L., Boss, E., Ackleson, S., Craig, S., Gregg, W., Lee, Z., Maritorena, S., Roesler, C., Rousseaux, C., Stramski, D., Sullivan, J., Twardowski, M., Tzortziou, M., Zhang, X., 2018. An overview of approaches and challenges for retrieving marine inherent optical properties from ocean color remote sensing. Prog. Oceanogr. 160, 186–212. https://doi.org/10.1016/j.pocean.2018.01.001.